Light-trapping nanostructures in ultrathin GaAs solar cells : towards a record efficiency

Master's Thesis

Romaric de Lépinau

June 23, 2016

LUND UNIVERSITY

LABORATOIRE DE PHOTONIQUE ET DE NANOSTRUCTURES

Abstract

Producing electrical power with photovoltaic solar panels is very attractive as the sun constitutes an inexhaustible source of clean energy. However, in order to make it a better alternative to other energy sources, its drawbacks must be addressed. In particular, scientific research is very active to find technologies that increase the efficiency of the solar cells, or decrease their cost. Reducing the thickness of thin-film solar cells would serve this second objective by reducing the amount of material needed. It also paves the way towards third-generation solar cells, e.g. nanowire solar cells, because the effective light-trapping techniques that are developed and implemented will be needed in those future devices. This master's thesis aims at implementing a theory of multi-resonant absorption to ultrathin GaAs solar cells. The absorption is based on resonant photonic and plasmonic modes, excited via a periodically nanostructured mirror at the rear side of the cell. A process for the fabrication of solar cells implementing such a nanostructured mirror was developed, and solar cells with simpler designs have already been made, with a 200 nm thick absorber. They have been characterized and exhibit quite high Fill-Factor (82 %) and open-circuit voltage (1.03 V) that are not degraded after transfer on another substrate, which is promising for the final cell. The short-circuit current exhibited a value of 16.1 $mA.cm^{-2}$ without anti-reflection coating, and with only a flat mirror at the rear side. Based on numerical simulations it is supposed to increase by 8.5 $mA.cm^{-2}$ with the addition of an Anti-Reflection Coating (ARC) and with the nanostructured mirror. Taking this contribution into account, we expect a short-circuit current of 24.6 $mA.cm^{-2}$ and an efficiency of 21 %, that have never been reached for such thin solar cells (200 nm). The process development is still ongoing for this final design, and we look forward to complete the fabrication of a device.

Preface

This project was carried out at 'Laboratoire de Photonique et de Nanostructures' (LPN), the photonics and nanostructures laboratory of the french national center for scientific Research (CNRS), between January and July, 2016. It is a degree project leading to a diploma of Msc. of Engineering, 'Engineering Physics' at LTH, Lund University. It is attached to the department of solid-state physics at LTH.

At LPN, the project is supervised by Dr. Stéphane Collin and Dr. Andrea Cattoni, CNRS researchers. At LTH, Dr. Magnus Borgström is the main supervisor and Dr. Carina Fasth is the examiner.

I would like to express my thanks to all the people that helped and guided me throughout this project. Stéphane Collin and Andrea Cattoni for having aroused my interest with such an exciting subject to work on. Julie Goffard, Hung-Ling Chen, and Jérôme Michallon helped me a lot with their experience in the subject, answering all my questions. They contributed to create an inspiring atmosphere in our office. Christophe Dupuis's help was priceless given his experience with cleanroom processes, from mechanical polishing to UV lithography and Scanning Electron Microscope. Carina Fasth and Magnus Borgström helped me review this thesis, and gave me precious practical information about the university's requirements. The ISE Fraunhofer Institute should also be thanked for their help concerning the layers' design and for supplying us with 4 high-quality epitaxial wafers.

This project is of course based on previous work at LPN, especially the multi-resonant absorption theory developed by Stéphane Collin, and the doctor's thesis of Nicolas Vandamme, who worked on the implementation of such mechanisms in ultrathin solar cells. My contribution is the adaptation of the process to the new epitaxial layers, and the realization of two working devices in the cleanroom, as well as their full characterization. I also optimized numerically the nanostructure geometry, to maximize the absorption.

Contents

Introduction

Background

The efficiency of a solar cell is the ratio of the electrical energy generated by the cell to the incident solar energy. A challenge in the photovoltaic research is to find a technology with the best compromise between low price per Watt of electricity produced, and high efficiency. Even though today's market is dominated by the cheap poly-silicon cells from China, other promising fields are explored that could increase the efficiency and lower the costs of production, such as thin-film solar cells with III-V materials. The very good optical and electrical properties of those materials allow for higher efficiencies and more perfect matching to the solar spectrum. In order to remain cheap enough to overcome its silicon counterparts, and because III-V elements are relatively expensive to grow, those solar cells must remain very thin to spend as little material as possible.

The project addresses the key issue of the production costs, as we propose to make an ultrathin solar cell made of gallium arsenide (GaAs), with an active layer 200 nm thick, one order of magnitude thinner than state-of-the-art devices (such as Altadevice's cell, [1]), thus saving even more material.

A key issue with thin film solar cells is that their thinness is detrimental to optical absorption. In order to enhance it, the mainstream strategy is to make textured interfaces in the cell, so that an incident beam of light is scattered in a random direction inside the active layer and thus travels a longer way and has more chance to be absorbed. This has already be adapted with success for 300 nm optically thin GaAs solar cells [2]. We will show that another approach based on the multi-resonant absorption is more relevant for ultrathin solar cells. This theory was developed at LPN and consists in activating resonant modes for the light inside the cavity formed by the active layers of the solar cell. It can be done with the help of a periodically nanostructured back mirror, which traps the incident photons inside the layers. Some similar approaches have already given encouraging results with ultrathin GaAs solar cells of 200 nm thick [3][4], with efficiencies up to 16.2 % and J_{sc} up to 22 mA/cm^2. They implement nanostructures at the front of the cell, and essentially act as a very efficient Anti-Reflexion-Coating (ARC), whereas we propose to implement a nanostructured back mirror.

Objectives

The main goal of my project is to fabricate an ultrathin solar cell with a nanostructured back mirror, characterize it, and observe enhanced performances. Intermediate goals consist in making a simple solar cell 'as-grown', on its substrate, and then a solar cell transferred onto a flat mirror. They are then fully characterized so that their performances can be analyzed and also to corroborate the predictions of a numerical model. The numerical results could then serve to estimate the performances of the final cell implementing a nanostructured back mirror. This work follows the PhD of Nicolas Vandamme who demonstrated numerically high absorption in ultrathin GaAs absorbers, and who proposed a proof-of-concept, a solar cell fabricated from an epitaxial stack from LPN ([5]). He also demonstrated high absorption in a 220 nm thick GaAs solar cell transferred onto a flat mirror [6]. The project differs from his work in the sense that the epitaxial wafer at my disposal is a different one, grown with specific technique, materials and dimensions. It comes from Fraunhofer Institute ISE, and state-of-the-art

performances are expected due to the high quality of their epitaxial layers. In the end, the solar cell will be a GaAs pn-junction with an AlGaAs Back-Surface-Field and an AlInP window layer as shown Figure 0.1. On top of it there will be a Si_3N_4 ARC, whose thickness will be tuned so that it helps activate the resonances. The role of those layers is further explained in section 1.1.

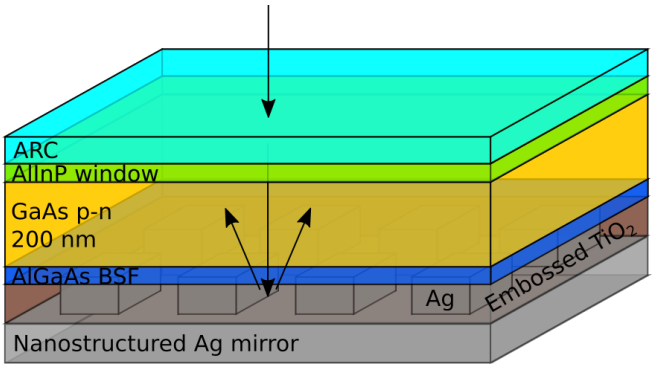

Figure 0.1: Optical representation of the desired solar cell. Adapted from [7]

A strategy was needed in order to reach the main objective, namely the fabrication of an ultrathin solar cell implementing the multi-resonant absorption, and which sports a record efficiency. First, two solar cells with simpler designs are made, to get familiar with the process and the characterization setups. Their optical performances are analyzed to verify their concordance with the numerical predictions. Then the numerical model is used to optimize the geometrical parameters that maximize the absorption in a solar cell with a nanostructured back mirror. The experimental results for the simplified cells are analyzed to identify eventual process steps that degrade the performances, and to predict the results of the final cell, based on the enhancement found numerically. At the same time, the process issues are addressed so that a solar cell with a nanostructured back mirror can be made.

In this master's thesis, the reader will first find information about solar cells and the light-trapping strategies used in the field, in particular the implementation of the multi-resonant absorption. It starts with a general introduction to the physics of solar cells, and in particular the electrical equivalent model of a solar cell, which is convenient to analyse experimental results. Different light-trapping strategies for thin solar cells will then be exposed, and we will compare their relevance for ultrathin solar cells. Some concept of the multi-resonant absorption theory will be exposed here, but not in detail as it is a complex theory and only its results were exploited for this project. To conclude this first part, the practical implementation of the multi-resonant scheme is exposed, as well as the numerical optimization of this implementation.

The second part deals with the fabrication of the solar cell. The structure of the cell is further detailed, and an outline of the whole process is given. This process can be simplified for the fabrication of the two intermediate solar cells. Preliminary to the fabrication of an actual solar cell, the main challenge is to develop and adapt a robust process and address unavoidable processing issues. We will expose how three different process steps were developed.

Finally, the results will be showed and discussed. The experimental result of the first two simplified designs can be compared with one another and will also help verify the relevance of the numerical model for the simulations. We will then try to extrapolate these experimental results to the final design, with the nanostructures, and discuss the performance improvement, with help of the numerical simulations.

After a conclusion to this report, the reader will find an appendix explaining further the numerical method used to simulate the optical absorption. Another appendix describes the characterization tools used to obtain the experimental results.

Chapter 1

Light trapping in ultrathin GaAs solar cells

1.1 Basics of solar cell operation

In order to understand the relevance of the light-absorption strategy implemented in this project, it is necessary to know the principles that guide the photovoltaic operation. This is done in this section, but more details explanations about the solar cells can be found on books like the one by Wurfel ([8]) or the one by Nelson ([9]), or on the website PVEducation.org ([10]). Most of the theoretical content in this part comes from those sources.

1.1.1 Light conversion in a semiconductor solar cell

The light source

In a photovoltaic solar cell, the light power is converted to an electrical power. Thus it is important to know precisely the properties of the light source. In this project, the solar cell performances are evaluated for terrestrial application, under direct exposure from the sun.

A rough model for the light source is to take a black body at a temperature of 6000 K, which is quite common to describe the solar spectrum. A refinement of this spectrum leads to the AM 0 standard, which is the solar spectrum as it can be detected outside the atmosphere. But the problem with this model is that it does not take into account the light absorption and scattering in the atmosphere.

To address that, the standard AM 1.5 G is commonly used, which is defined by the American Society for Testing and Materials (ASTM). It corresponds to the spectral irradiance from the sun, after taking into account the effect of the atmosphere (AM stands for *Air Mass*). The 1.5 factor represents the light path enhancement due to the angle of incidence of the sun rays entering the atmosphere at the average latitude of the U.S.A., 48.2 °from the zenith. It is displayed in Figure 1.1. This spectrum integrated over all wavelengths amounts to 1000 W/m^2 which is an important order of magnitude to keep in mind when working with solar conversion devices.

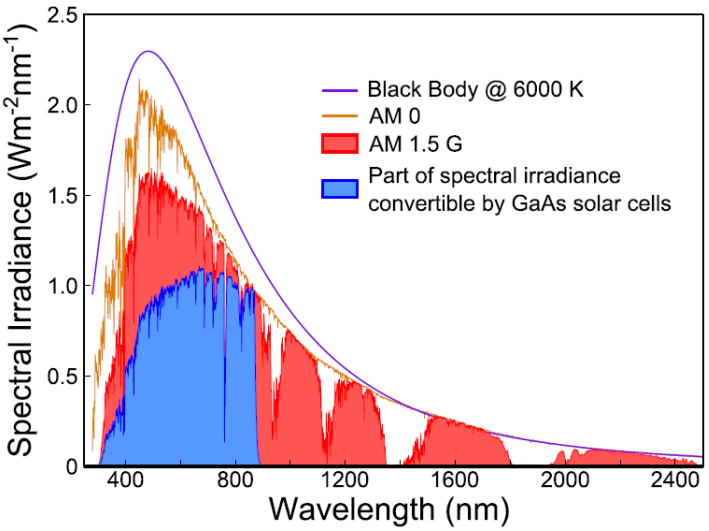

Figure 1.1: Solar spectral irradiance $\Phi(\lambda)$ outside the atmosphere (AM0) and at the earth's surface (AM1.5G), along with a black body at 6000 K. The power density available for photovoltaic conversion in GaAs is in blue. From [5].

Band-to-band absorption in a pn-junction

As of today, most of the commercial solar cells are made out of a semiconductor material (e.g. Silicon, Si), or a semiconducting alloy (e.g. Gallium Arsenide, GaAs). In those materials, the energy levels of the electrons are restricted to some bands, separated by a bandgap. The upper band is referred to as the conduction band, and the lower one is the valence band. The valence band states are mostly populated by electrons, and the conduction band states are mostly empty. If an electron reaches the conduction band, it is free to spatially move in the material, as it will find a lot of available states. Similarly, an absence of electron in the valence band is called a hole and can also move almost freely. Those electrons and holes are charge carriers and can participate in the electrical transport.

This population can be described by a Fermi distribution, centered at an energy called the Fermi level, usually in the bandgap. The closer the Fermi level is to the conduction band, the more electrons there are in the conduction band. The same goes for holes in the valence band. The semiconductors can be doped to change the carrier population in the band, and displace the Fermi level, by introducing impurities in the material. Gallium Arsenide is a III-V material, which means that it is equally composed of elements from the third column of the periodic table (Ga) and the fifth (As). As a consequence the average valency in the material is 4. By substituting elements from the fourth column (e.g. Si) to Ga or As, this valency is changed, either increased or decreased. With an excess of donors, i.e. of elements of valency 5, the material is called n-doped, and it will naturally have more electrons in the conduction band. An excess of acceptors, elements of valency 3, leads to more holes in the valence band.

In order to have a current flowing, the generated charges must be separated and driven toward two opposite contacts. This is the role of a pn-junction. This is illustrated Figure 1.2 where a p-doped material and a n-doped material are joined together to form a so-called *pn-junction*.

The pn-junction creates a depletion zone at the interface between the p- and n- layers, depleted of free carriers. As a consequence, ionized fixed atoms stand in this zone, which generates an electric field that drives the charges toward the junctions extremities. The electrons are repelled toward the n-side, and the holes toward the p-side, where they are collected by electrical contacts.

A photon incident at an energy above the band gap can excite an electron from the valence band and promote it to the conduction band. An electron-hole pair is then created and can participate to the current flow in the device. This process is illustrated by the green arrow on Figure 1.2. Two limitations to the solar efficiency can be identified at this stage. First, the photons whose energy is lower than the energy gap of the material are not absorbed, they see a transparent media. Then as for electrons whose energy is beyond the energy gap, they generate an electron-hole pair which rapidly relaxes thermally to a potential corresponding to the bandgap energy. The only part of the solar spectral irradiance available for conversion with a GaAs solar cell is thus represented in blue on the solar spectrum Figure 1.1.

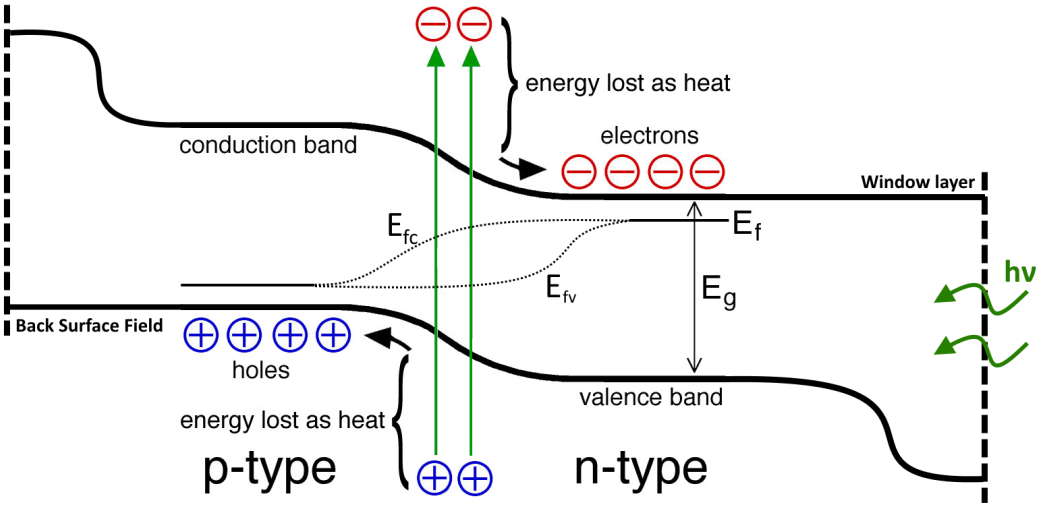

Figure 1.2: Mechanism of charge generation and separation in a pn-junction. Adapted from *http://education.mrsec.wisc.edu*.

As pairs are generated by light absorption, the population of both type of carriers increases and should now be described by two Fermi distributions, centered around two 'Quasi-Fermi' levels that are represented by the dotted line Figure 1.2.

For a detailed introduction to semiconductors, see for example Sze [11], or also Nelson [9] or Wurfel [8] which are more specifically related to solar cells.

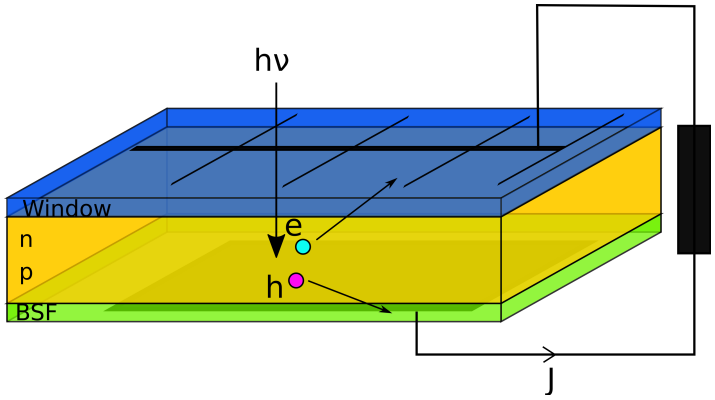

Figure 1.3: Typical solar cell structure.

Another noticeable feature in Figure 1.2 is the presence of two different materials at the ends of the junction, also represented on the sketch Figure 1.3. Those barrier layers are important for photovoltaic applications to prevent the minority carriers (electrons on the p-side and holes on the n-side) to reach the surfaces where they could recombine with majority carriers and reduce the current generated. Indeed, in these regions the bending of the band constitutes a potential barrier for the minority carriers. They are also called 'Selective contacts'.

In accordance with the cell design adopted in this project, the photons enter the cell by the n-side, where the barrier layer is called *Window layer*. Its bandgap energy is high enough (2.3 eV, corresponding to a wavelength of 540 nm) to be transparent for most of the light spectrum, and it repels holes from the surface. The barrier at the rear of the cell is called the Back Surface Field (BSF) and also exhibits a potential barrier in its band structure to repel electrons from the back surface.

1.1.2 Electrical model and parameters

The solar cell can be modelled by a simple equivalent electrical circuit where the components include some sources of loss or of recombination in the junction, see Figure 1.4. It allows to introduce important parameters for solar cell performances and discuss their physical origin.

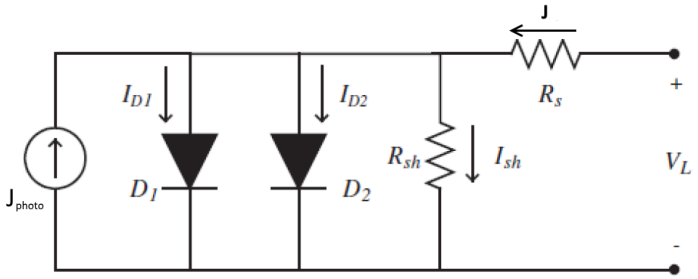

Figure 1.4: Equivalent electrical circuit using the double diode model. From [5].

Let us analyze each electrical component in the model from left to right. First, there is an ideal current generator. It corresponds to the photo-generated current.

There are two diodes in this model. While a pn-junction is well described electrically by a single diode, a double-diode model allows to better describe the recombination mechanisms at stake in the cell. The ideality denoted n is an additional parameter in the denominator of the exponential in the diode equation, that represent the type of recombination.

The recombination mechanism is the destruction of an electron-hole pair, either to give rise to a photon (radiative recombination), or to release energy which is thermally lost (non-radiative recombinations). Non-radiative recombinations can occur via impurities that introduce intermediate energy levels between the quasi-Fermi levels. In the junction, many carriers of both types are generated, and there is no dominant population such as in the bulk. This situation is called *high-level injection* and in this case, recombination mechanisms are well described by diode characteristic with an ideality factor n=2 [8]:

$$J_{nr} = J_{02}\left(\exp\left(\frac{q(V - J_{dark}R_s)}{2kT}\right) - 1\right)$$

Those non-radiative recombinations are detrimental to the performances and arise directly from the material quality. J_{02} should be as small as possible for high performances. Another non-radiative

type of recombination is the Auger recombination and it is negligible in GaAs.

Radiative recombinations as well as non-radiative recombinations at the surfaces, where there is a carrier majority, are well described by a standard diode characteristic, with an ideality of 1.

$$J_r = J_{01}\left(\exp\left(\frac{q(V - J_{dark}R_s)}{kT}\right) - 1\right)$$

We also want J_{01} as small as possible for high performances. Apart from those recombination mechanisms intrinsic to the pn-junction, there are some loss channels in a solar cell. Resistive losses can be the resistance between the semiconductor and the metallic contact, and in the metal contact themselves, along with the resistance of the last semiconducting layer in which the carriers travel to reach the metal contact grid. They are well modeled by a series resistance, denoted R_s in Figure 1.4. R_s should be as small as possible.

Finally, leakage currents in the junction are represented by a parallel or *shunt* resistance, R_{sh}. Such currents can originate from leakages around the sides of the device or through the layers via defects. R_{sh} should be as high as possible.

The current equation for this double-diode model is:

$$\begin{aligned} J = J_{01}\left(\exp\left(\frac{q(V - JR_s)}{kT}\right) - 1\right) - J_{photo} \\ + J_{02}\left(\exp\left(\frac{q(V - JR_s)}{2kT}\right) - 1\right) + \frac{V - JR_s}{R_{sh}} \end{aligned} \tag{1.1}$$

A common approximation consists in adding the constant photo-generated current J_{photo} to the dark current J_{dark}, solution of (1.1) without J_{photo}. This allows to relate the dark IV characteristic to the illuminated IV characteristic by simply shifting the curve along the y axis. Such a current-voltage characteristics under illumination is plotted in Figure 1.5.

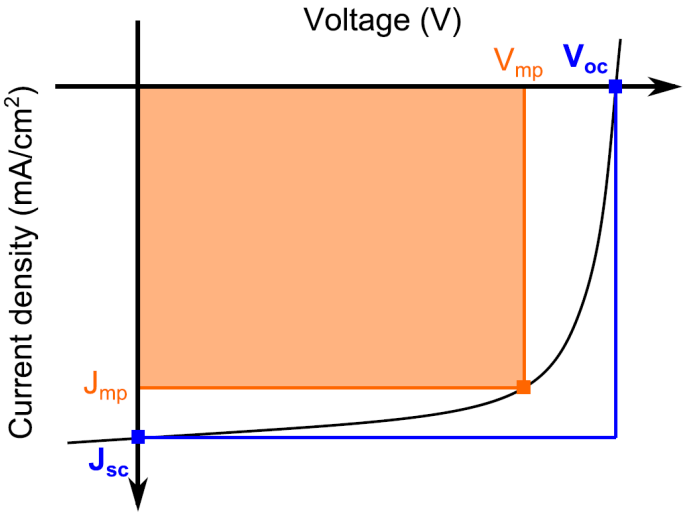

Figure 1.5: Characteristics of a pn-junction diode under illumination. From [5].

Four important parameters can be extracted from an IV-curve.

First, the short-circuit current, J_{sc}. It represent the current flowing in the device without external bias, only due to the photogenerated current. It is closely related to the External Quantum Efficiency:

$$EQE(\lambda) = \frac{\text{Number of collected electrons}}{\text{Number of incident photons}(\lambda)} \tag{1.2}$$

By integrating the spectral photon flux per unit area over all wavelengths, weighed by the EQE, one obtains an expression for the short-circuit current density:

$$J_{sc} = q_0 \int_0^\infty EQE(\lambda) \cdot \frac{\lambda \cdot \Phi(\lambda)}{h \cdot c_0} d\lambda \tag{1.3}$$

Where q_0 is the elementary charge, h the Planck constant, c_0 the speed of light in vacuum. The quantity $\frac{\Phi(\lambda)}{h \cdot c_0}$ is the spectral flux of incident photons and is expressed as a number of photons per wavelength per second per unit area. The irradiance Φ is usually the standard AM 1.5 G.

The EQE can be decomposed as follow :

$$EQE(\lambda) = \underbrace{\frac{\text{Number of collected electrons}}{\text{Number of generated electrons}}}_{\text{IQE}} \cdot \underbrace{\frac{\text{Number of generated electrons}}{\text{Number of incident photons}}}_{Abs} \tag{1.4}$$

This second ratio is the optical absorption in the material, assuming that every absorbed photon creates an electron-hole pair, which is the case for a semiconductor.

The first ratio is the Internal Quantum Efficiency (IQE) and represents the charge collection efficiency. It should be very close to 1. The reasons why a charge carrier would not be collected is that it recombines before. For the numerical simulations, we assume that IQE=1, so that the expression of the EQE is only the optical absorption. This allows to simplify the expression of J_{sc} by replacing $EQE(\lambda)$ by $Abs(\lambda)$. This calculation will be done for every layer in the numerical simulations to evaluate the shortfall in term of photo-current due to the absorption in each layer.

At open-circuit, the solar cell exhibits a voltage, V_{oc}, due to the accumulation of photo-generated carriers at the contacts. As the Fermi levels are close to the edges of the bands, V_{oc} is limited by the bandgap energy :

$$qV_{oc} \leq E_{gap}$$

The product $J(V) \cdot V$ is the power that can be extracted from the device. It presents a maximum, which is the working point of a solar cell. The Fill-Factor is a measure of the squareness of the curve, it is defined as:

$$FF = \frac{(J(V) \cdot V)_{max}}{J_{sc} V_{oc}} \tag{1.5}$$

It should be as high as possible, and it is limited by the series resistance that tends to lower V_{mp}, and the shunt resistance, which lowers J_{mp}. High saturation currents J_0 also lower the FF.

Last but not least, the efficiency of a solar cell is the ratio of the electrical power collected to the solar power incident on the device (Φ). It depends on the light source considered. It can be expressed with the previous parameters:

$$\eta = \frac{FF \cdot J_{sc} \cdot V_{oc}}{\Phi} \tag{1.6}$$

This project is about making ultrathin solar cells, so the challenge is to absorb light in a small volume. The key parameters involved are thus the EQE and consequently, the short-circuit current.

1.2 The multi-resonant absorption

1.2.1 Light-trapping strategies

In order to increase the optical absorption, different strategies exist and are commonly used in the photovoltaic field. Three different approaches will be discussed, which correspond to the sketches presented in Figure 1.6.

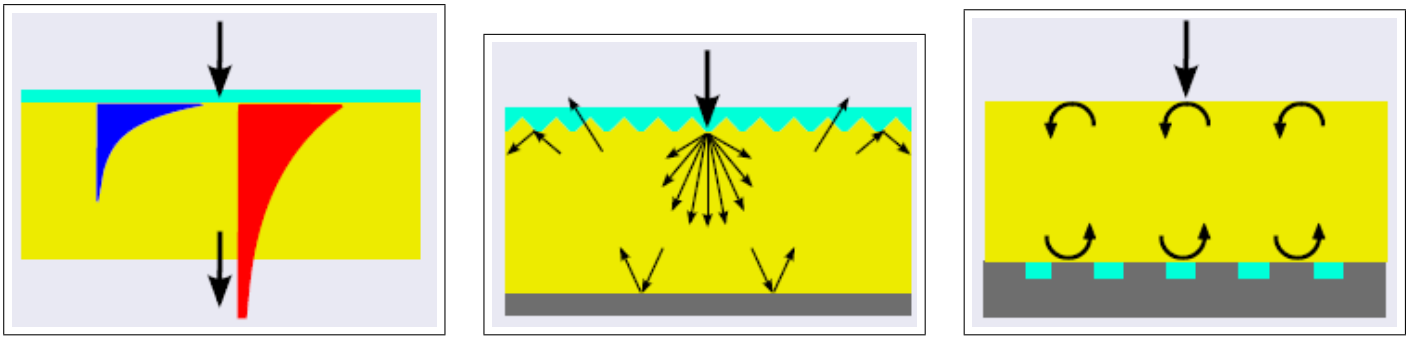

(a) Single-pass absorption with perfect Anti-Reflection-Coating (ARC).

(b) Lambertian scattering with perfect ARC.

(c) Multi-resonant absorption.

Figure 1.6: Light absorption strategies. Adapted from [12].

The first approach simply relies on the use of an Anti-reflection-Coating (ARC). It is basically a transparent material whose index and thickness are tuned so that destructive interferences occur for incident light at a certain frequency. Broadband ARC can be achieved with multi-layers or nanostructured front surfaces. As a consequence, the reflection at the surface is lowered. To illustrate this type of absorption, the intensity in a semi-infinite medium of absorption coefficient α is calculated. The intensity follows the Beer-Lambert law of absorption, with an exponential decay ([9]):

$$I(x) = I_0 \cdot e^{-\alpha x} \qquad \text{with the absorption coefficient} \qquad \alpha = \frac{4\pi \mathrm{Im}(\overline{n}))}{\lambda} \tag{1.7}$$

The normalized absorption probability in a solar cell of thickness d with a perfect ARC is then :

$$Abs(\lambda) = 1 - e^{-\alpha(\lambda)d} \tag{1.8}$$

A second approach is more effective and consists in using a textured interface to scatter light in all directions inside the cell. A perfect mirror at the back of the cell is considered. The advantage of this strategy is a major path enhancement F, theoretically established by Yablonovitch [13]:

$$F = 4 \times n_R^2 \qquad \text{with} \qquad n_R = Re(\overline{n}) \tag{1.9}$$

This path enhancement originates from an enhancement of n_R^2 of the electric field intensity inside a medium of refractive index n_R, compared to the one in the incident medium. This is a consequence of the density of optical states being proportional to n_R^2. One of the factor 2 comes from the integration

of all the possible escape angles for a photon inside of the slab, which is limited by the texturation and the use of an ARC. The other factor two simply originates from the use of a perfect back mirror, preventing the escape of photons on the backside.

This is of course an upper theoretical limit and it has not yet been reached with actual solar cells.

The absorption in a slab of material of thickness d cannot be higher than the Lambertian limit [12] [14]:

$$Abs(\lambda) = \frac{\alpha(\lambda)d}{\alpha(\lambda)d + \frac{1}{F}} \tag{1.10}$$

This random scattering of light is often the strategy used for the most efficient thin-film devices. But it may not be optimal for ultrathin solar cells. A reason is that the typical height of the texturation is typically a hundred of nanometers, which would be about the thickness of an ultrathin solar cell, making it hard to implement. Another reason is that the thickness of the cell would fall below the wavelength of the light, where ray optics is not valid anymore. As the demonstration of 1.9 is based on a geometrical-optics derivation, it does not hold for sub-wavelength structures. It also implies a weakly absorbing medium, typically silicon, whereas efficient absorbers such as gallium arsenide are wanted in ultrathin solar cells.

The last approach looks more promising for ultrathin solar cells. It consists in the activation of resonances with the help of periodic structures. The mechanisms at stake in such a structure will be explained in the next part, but the maximum absorption attainable is higher than for the two previous methods.

The best improvements in terms of absorption concern very thin absorbing layers. Typically, in a 25 nm thick GaAs layer, the absorption probability with a multi-resonant mechanism is nearly 1 for wavelengths below 700 nm, whereas at the lambertian limit, the absorption decreases after 450 nm, as it is plotted in Figure 1.7. This is already well above the single-pass absorption in such a layer.

As for the 200 nm thick absorbing layers that we propose to make, the benefit in term of absorption is not as high as for 25 nm, but the reasoning about the thickness compared to the typical size of the texturations and the fact that ray-optic demonstrations are not valid at those wavelengths still hold.

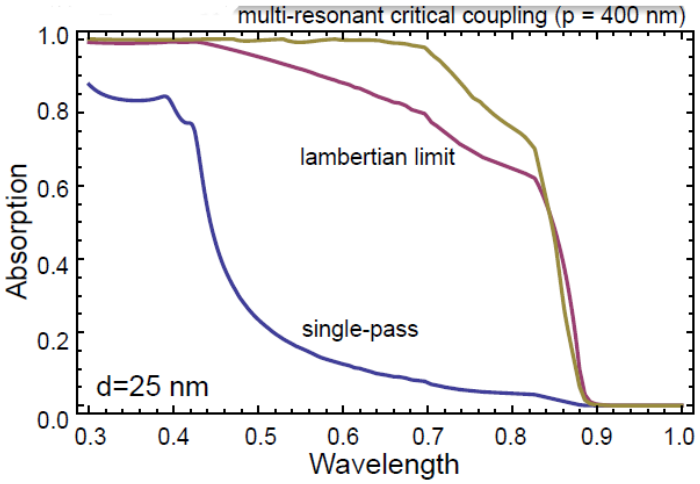

Figure 1.7: Maximum theoretical absorption in a 25 nm thick GaAs slab with different light-absorption strategies. Wavelengths are in μm. From [12]

1.2.2 Coupling to resonant modes

The multi-resonant theory was developed at LPN by Stéphane Collin. The results of importance for this project are exposed in this part, and mostly come from his conference at C2N [12]. It consists in coupling an incident wave to a periodic grid whose period is smaller than the wavelength of the light source.

The three main categories of resonances activated by sub-wavelength gratings are exposed in Figure 1.8.

First, the Fabry-Pérot resonance consists in which the wave is internally reflected multiple times. A condition on the index of the slab, its thickness and the wavelength of the signal causes destructive interferences of the reflected light. As a result, a standing wave is trapped in the slab. The first condition for total absorption is that the dephasing upon one round trip of light in the cavity is a multiple of 2π so that the light remains trapped in the cavity. Moreover, the reflection coefficients at the interface between the incident medium and the slab must be tuned so that the reflected wave interferes destructively with the sum of the waves that escape the slab.

Waveguide modes can also be activated when the in-plane wave-vector of the incident wave that diffract on the structure (the grating brings 'in-plane momentum') matches one of the guide. Those guided modes exist due to total internal reflection in the slab.

Finally, some localized modes spatially limited around the structures are also activated. They are often coupling effects between the electromagnetic wave in the transparent layers and an electron displacement in the metal below. Such phenomena are called Surface Plasmon Polaritons (SPP) or Localized Surface Plasmons (LSP).

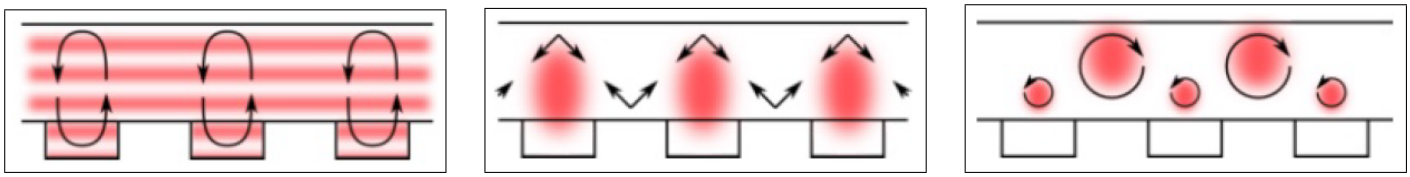

(a) Fabry-Pérot. (b) Waveguide. (c) Localised modes.

Figure 1.8: Different types of resonance that can typically exist in our structures. From [5].

For all these types of resonance, their influence on the absorption can be modeled by independent Lorentzian shaped functions. The absorption probability of a photon by a resonant mode is:

$$Abs_m(\omega) = \frac{4\gamma_r\gamma_{nr}}{(\omega-\omega_0)^2 + (\gamma_r+\gamma_{nr})^2} \tag{1.11}$$

γ_r and γ_{nr} are, respectively, the radiative decay rate, due to specular reflection, and the non-radiative decay rate which come from absorption in the medium. When those parameter equalize, the absorption reaches unity at its central frequency, ω_0. It is the critical coupling condition.

The probability for a photon to be reflected by coupling to one mode is $1 - Abs_m$. As those probabilities are independent, the total reflection probability is their product:

$$R = 1 - Abs(\omega) = \prod_m (1 - Abs_m(\omega)) \tag{1.12}$$

This expression leads to an absorption curve such as in Figure 1.9 (top blue line). The coloured functions are the contribution of each resonance, with a Lorentzian shape.

As the objective is to maximize the absorption, the mode separation $\delta\omega$ should be as low as possible. To do so, many modes should be activated by the structure. This can be optimized by tuning the geometrical parameters of the array. The resonance width, $\Delta\omega$ should be as large as possible, to maximize the overlap between the resonances. Mathematically, the full width at half-maximum of a Lorentzian function (1.11) is proportional to the total decay rate $\gamma_r + \gamma_{nr}$, that should thus be maximized.

In a real structure, the shape of the absorption would exhibit some peaks, like in Figure 1.9. But as the resonant modes are not necessarily in a critical coupling condition, the peaks would not reach 1. And as they are coupled with each other in a complex way, the overall shape of the absorption will not be a nice sinus-like wave such as the blue curve.

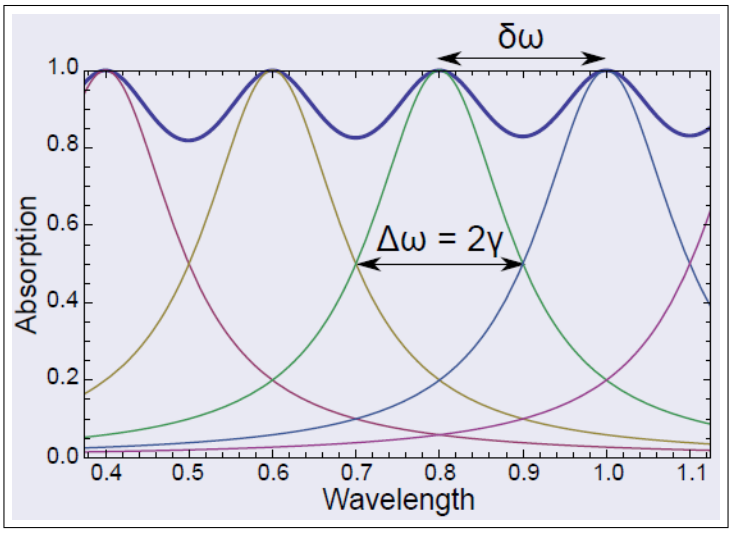

Figure 1.9: Absorption of overlapping independant resonant modes.

In this section, the importance of light trapping strategies in ultrathin solar cells was highlighted. The multi-resonant absorption seems to be promising and relevant, as it shows extremely high theoretical absorption limits, and could be practically implemented in a real device.

1.3 Implementation of a multiresonant nanostructured solar cell

1.3.1 Design of the structures

The multi-resonant absorption strategy with the help of periodic nanostructures is a very promising way to increase the optical absorption in ultrathin solar cells. As the aim of this project is to make an actual solar cell, a design must be elaborated that implements and optimizes the multi-resonant absorption. This design corresponds to the sketch in Figure 1.10 and consists in a silver back mirror nanostructured with a grid of square nanoplots. This mirror is embedded in TiO_2.

Silver is chosen for its high reflectivity, higher than 90 % for the wavelengths from 450 nm to 900 nm. But it is not a perfect electrical contact because there is a poor match between the work function of silver and the Fermi level in the semiconductor, which is detrimental to the charge collection.

But an alternative technique consists in implanting periodically some small metallic contacts in the mirror. Gold and titanium typically make for efficient ohmic contacts. A high electrical collection is thus maintained, while the optical properties of the structures are not altered too much since those localized contacts only cover 1% of the surface. This is more detailed in section 2.1.2.

TiO_2 serves as a mold for the Ag plots during the fabrication process. It is also a material of choice for coupling the light with the structures since it has a high refractive index (about 1.9).

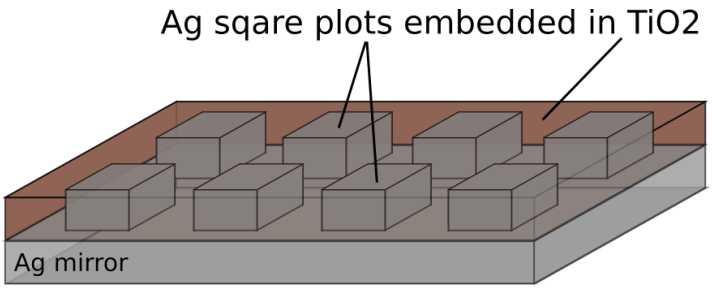

Figure 1.10: Actual design of the periodic nanostructured back-scatterer.

1.3.2 Numerical optimization of the nanostructures

In order to reach the critical coupling condition and maximize the overlap between the resonances, the geometrical parameters of the nanostructures must be tuned accordingly. This is done numerically, using the program *Reticolo* which can simulate the optical absorption in each layer of the device.

A more detailed explanation about the operation of Reticolo is given in Appendix A.

The software computes the value of the electric field everywhere in the material. By taking the divergence of the Poynting vector $\vec{S} = \vec{E} \times \vec{H}^*$, one can deduce the absorbed power per unit volume per frequency, P, at a certain point in the material [15]:

$$P(\mathbf{r}, \omega) = \frac{1}{2}\mathrm{Re}(\mathrm{div}(\vec{S})) = \frac{\omega \mathrm{Im}(\epsilon(\mathbf{r}, \omega))}{2} |\vec{E}(\mathbf{r}, \omega)|^2 \tag{1.13}$$

where $\epsilon(\mathbf{r}, \omega)$ is the permittivity of the material, $\vec{E}$ the electric field and $\vec{H}$ the magnetic field.

By integration of this quantity over the whole volume of a layer, the power absorbed in this layer at this frequency is deduced. It is normalized by the incident power to give a probability of absorption in the layer, at a given wavelength. The simulation runs for a given set of wavelength, to plot a curve that displays the absorption probability versus the wavelength. See for example the results of Figure 3.14.

For each absorption curve calculated with the software, an equivalent contribution to the short-circuit current is always displayed. It is expressed in $\mathrm{mA/cm^2}$. The EQE is replaced by the absorption as discussed in 1.1.2. This current contribution is then :

$$J = q_0 \int_0^\infty A(\lambda) \cdot \frac{\Phi(\lambda)\lambda}{h \cdot c_0} d\lambda \tag{1.14}$$

$\Phi(\lambda)$ is set to be the standard AM 1.5 G.

In all the simulations realized, the electrical contacts and layers were intentionally omitted, considering the fact that they have a very small coverage of the surface and thus do not alter too much the

optical absorption. Moreover, as their periodicity is much larger than the one of the nanostructures, a too high resolution would have been needed for the simulation.

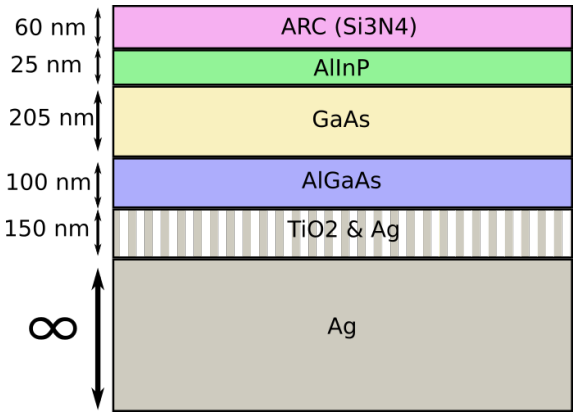

(a) Successive layers defined in the software Reticolo.

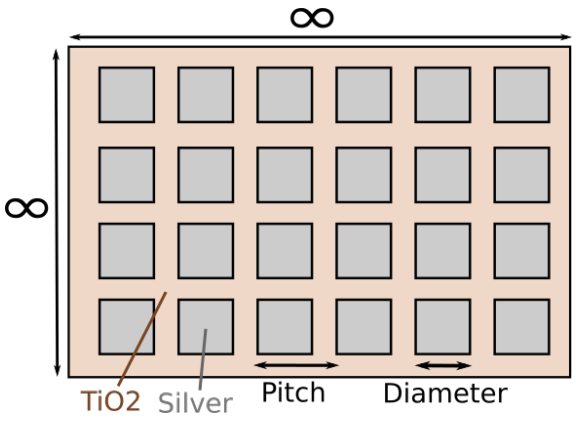

(b) Geometry and parameters of the structured layer in the software Reticolo.

Figure 1.11: Geometrical input parameters for the calculation of the optical absorption

The different input parameters for the optimization of the structured array were the period of the structure, p, the thickness of the structured layer, h, and the Ag-TiO_2 length-ratio LR, defined as the ratio of the diameter of the silver plots and the period : $LR = \frac{D}{p}$.

The optimization problem consists in maximizing the absorption in the GaAs layer (maximizing J_{GaAs}), with respect to the 3 variable parameters p, LR and h. First, the variable LR is fixed and p and h are concurrently optimized. Then those two parameters are fixed and LR was optimized. This method is iterated 1 time to get closer to a local maximum.

The best result are achieved with the parameters in Table 1.1, which lead to a theoretical current $J_{GaAs} = 24.0$ mA.cm^{-2}

Period (nm)	Length-Ratio	Height (nm)
700	0.6	0.13

Table 1.1: Parameters of the nanostructures array which gave the best numerical result

The result of this simulation is described and detailed section 3.3.

Chapter 2

Ultrathin solar cell fabrication

2.1 Fabrication process of a device

For this project, the epitaxial layers were already grown, but I processed them through each process step by myself, except for the metal depositions which were performed by someone else at the lab. I have also developed and optimized some steps of this process, and three of them will be shown.

2.1.1 The epitaxial layers

		Thickness (nm)	Doping (cm-3)
p GaAs	Contact	300	9,00E+18
p Al0,4GaAs	BSF	100	2,00E+18
p GaAs	Base	100	1,00E+18
i GaAs		5	
n GaAs	Emitter	100	1,00E+18
n Al0,61InP	Strained window	25	2,00E+18
n In0,13GaAs	Cap (Si) layer	100	5,00E+18
n GaAs	Cap (Si) layer	250	9,00E+18
n Al85GaAs	Etch stop	300	1,00E+18
n GaAs	Buffer	250	5,00E+18
GaAs	Substrate	Approx. 500 µm	doped

Figure 2.1: Epitaxial layers structure of the wafer C2853 from ISE Fraunhofer institute

The wafer on which the solar cells are designed was epitaxially grown at Fraunhofer institute ISE, Germany. This wafer is different from the previous ones used at the laboratory (grown in RCAST, University of Tokyo, Japan, and also at LPN). First, it was grown using the Metal-Organic-Vapor-Phase-Deposition (MOCVD) technique, whereas the ones from LPN were grown with a Molecular Beam Epitaxy technique (MBE). With MBE, there is a very precise control over the thickness of the deposited material, which allows for high quality interfaces. As of today, MOCVD is more industrially viable and it allows for high crystal quality and precise control of the doping levels[16]. Those MOCVD layers are

also very promising compared to the MOCVD ones from RCAST, since they come from Fraunhofer Institute, ISE, which is renown for their high-efficiency solar cells based on their epitaxy of III-V materials. In particular, they hold the world record for solar cell efficiency, at 46.0 % for a four-junction solar cell under light concentration [17]. ISE is equipped with semi-industrial dedicated MOCVD machines, able to produce very high-quality layers. It might indicate that the defect concentration is especially low and that the doping levels are tuned with high precision. They also master the growth of AlInP as a window layer, which benefits III-V solar cells performances [18].

The layers are shown in Figure 2.1. The substrate is about 500 μm thick and is n-doped. On top of it is an AlGaAs layer, with an aluminum content of 85%. It acts as a stopping layer during the removal of the substrate, later in the process, due to the selectivity of the etchants. Then comes a contact layer, highly n-doped to enhance the conductivity. It also acts as a *cap layer*, a layer whose lattice parameter compensates for the constraints induced by another layer, in our case, the AlInP layer. Then, there is another cap layer of InGaAs, and the AlInP window layer, with 61% of Aluminum. The pn-junction is 205 nm wide and there is a 5 nm thick intrinsic GaAs layer in the middle, that is assumed to be there for practical reasons during the epitaxy. The Back Surface Field layer (BSF) is 100 nm thick and is made of $Al_{0.4}Ga_{0.6}As$. Finally, the bottom contact layer, which is at the top of the stacks for the moment, is a p-doped 300 nm thick GaAs layer.

2.1.2 Outline of the process

The process is described in Figure 2.2. It represents an overview of the technological steps required to make a solar cell out of the previously described wafer. All those steps were performed as part of the project, in the cleanroom at LPN.

The localized ohmic back contacts are first defined via UV lithography using a negative resist. The photo resist is patterned with an array of square plot contacts (5×5 μm), of period 50 μm. There as thus made very close to one another, but do not cover a large area which allows a large portion of the light to reach the mirror. It is thus a good trade-off between optical and electrical performances.

The resist serves as a mask for the deposition of the metal via Electron Beam Physical Vapor Deposition (EBPVD). 20 nm of Titanium are deposited as an adhesion layer followed by 200 nm of Gold. A subsequent lift-off removes the resist along with the undesired metal. The metallic contacts are then used as a mask for the wet chemical etching of the GaAs contact layer (Figure 2.2b).

As for the nanostructure definition, the TiO_2 sol-gel is spin-coated on the surface of the sample, so that a uniform liquid layer of about 100 nm thick is formed. A PDMS stamp is immediately placed on top of it (see Figure 2.2c) to pattern the sol-gel with a grid of nanoplots. This nanoplot structure looks like a saw-type structure on the 2-D sketches. The sample is annealed at 110 °C for 5 minutes to desorb the solvents from the sol-gel solution and solidify it. The nanostructures on the stamp are thus transferred to the TiO_2 layer.

A 200 nm thick Ag mirror is then deposited via EBPVD, with a rotation of the sample at an angle of 30° inside the evaporation chamber to ensure a conformal deposition between the structures and the localized contacts. The metal fills the nanoplots and make an actual nanostructured Ag mirror. A 20 nm thick Chromium layer is then deposited to enhance the adhesion with the polymer later on.

The next step is the transfer on a glass substrate. A 1 mm thick glass slab is first coated with a primer (adhesion enhancer). A commercial polymer, Ormostamp©, is coated on the top of the sample (mirror side), and the glass slab is bonded onto it. The sample is placed under a UV lamp for 20 minutes to harden the polymer (see Figure 2.2d).

The thick substrate is etched away in three successive chemical solutions. The first one exhibits a fast etching rate and is not selective on the etch stop layer, while the last one has a slow etching rate

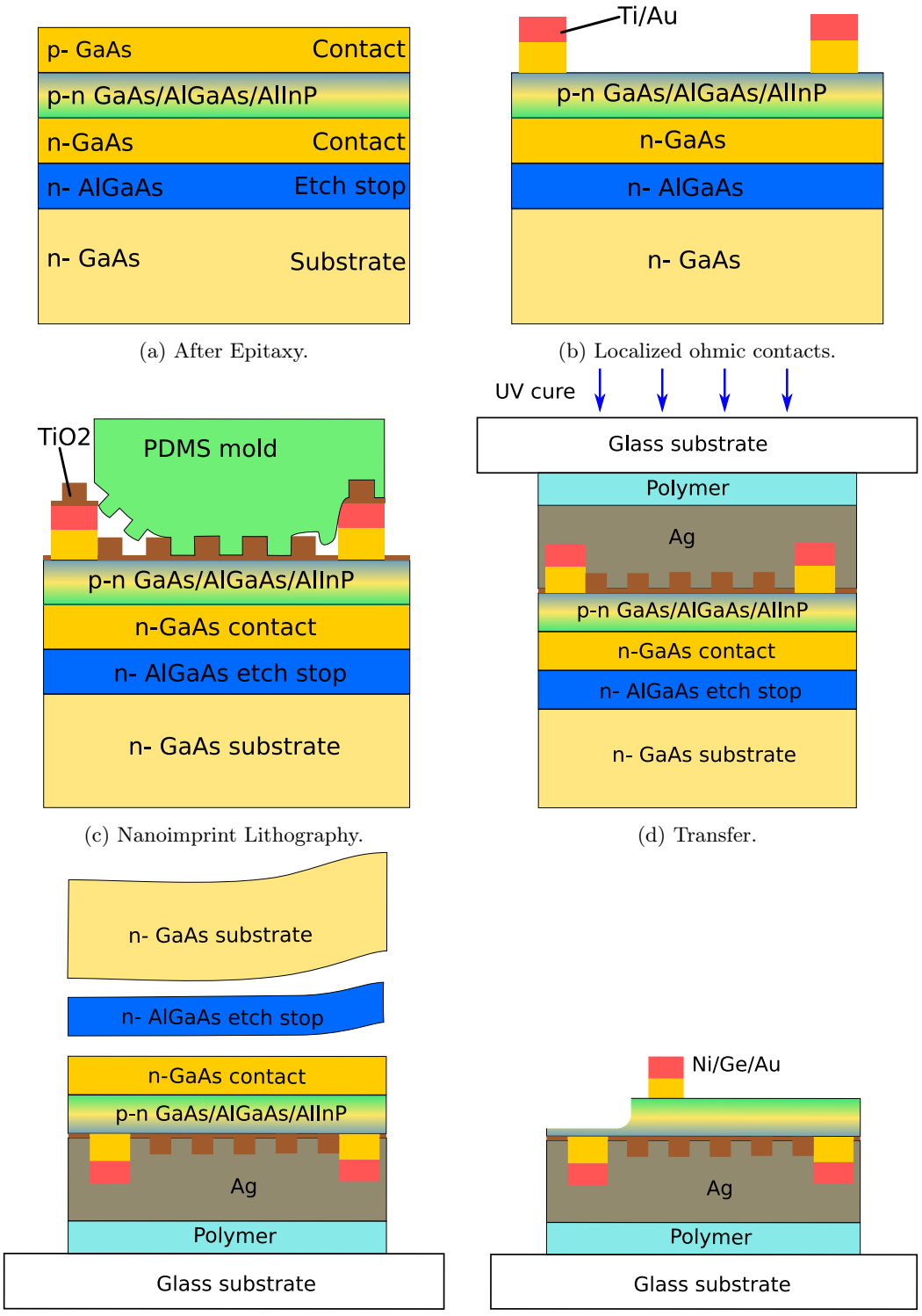

(a) After Epitaxy.

(b) Localized ohmic contacts.

(c) Nanoimprint Lithography.

(d) Transfer.

(e) Substrate removal (upside down).

(f) Front contacts design and mesa definition.

Figure 2.2: Fabrication process. Adapted from [5], Fig. 90

but is very selective on the etch stop layer, see details in 2.2.2. The second solution presents etching properties in between. This method ensures a quite fast and uniform etching, while keeping a high selectivity from the etch stop layer to not risk etching the important layers. The etch stop layer is then removed in diluted HF, which is very selective for the etching of AlGaAs from GaAs [19] (see Figure 2.2e).

Finally, the front contacts are patterned the same way as the back ones, only the composition of the metallic contacts differs. Due to the n-doping of this side of the wafer, gold is associated with nickel and germanium to make an efficient ohmic contact. In order to delimit square diodes (individual solar cells on a sample will be called diodes) on the sample, the pn-junction is etched to define squared mesas (on the left, in Figure 2.2f). The geometry of the front contacts and the mesas of the cell can be seen in Figure 2.3.

An additional step would consist in depositing an Anti Reflection Coating (ARC) on top of the final layer. It is made out of Si_3N_4 and is 60 nm thick. This layer whose optical index is known is here to prevent reflection at the entrance of the light in the device, and help coupling the light to the resonances in the device.

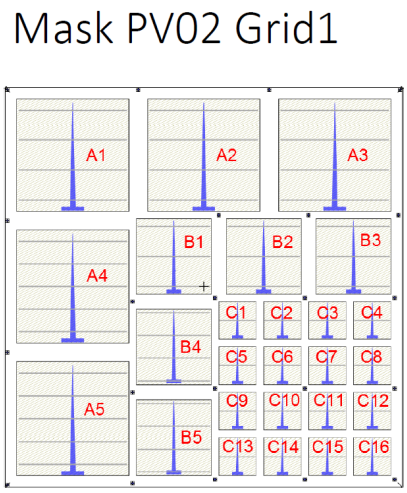

Grid 1	Suqare (mm)	Spacing (µm)	Surface mesa (cm²)	Uncovered surface (cm²)	Shadding (%)
AAA	10	800	1	0,9513	4,87
AA	5	600	0,25	0,2371	5,15
A1-3	3	800	0,09	0,08572	4,76
A4-5	3	600	0,09	0,08535	5,17
B1-3	2	800	0,04	0,03795	5,12
B4-5	2	600	0,04	0,03780	5,51
C1-16	1	600	0,01	0,009371	6,29

Figure 2.3: Top view and geometric parameters of the mask used for the front contacts definition (blue T-shapes with the transverse lines) and the mesa definition (light grey squares)

2.1.3 Simplified process for simplified cells

Two cells with simplified designs have also been realized to help elaborating the process and to compare the performance improvements.

The first cell made is not transferred onto another glass substrate, and does not have any nanostructures. It is called 'as-grown'. The process is thus simplified and the steps 2.2c, 2.2d and 2.2e are omitted. It will serve to get familiar with the process and evaluate the performances of the epitaxial The rest iided by Fraunhofer ISE.s identical except that the fro stack provnt contacts are on the top of the stack, thus on the p-doped side, and the back contacts are on the bottom of the substrate, n-doped. To match the work functions of the metal contacts with the Fermi level inside the semiconductor, the metal alloys are switched.

The second cell is more complex. It is a cell with a silver back mirror, transferred onto a glass substrate, but without any nanostructures. The photons thus see a flat silver mirror. The process is

the same as for the nanostructured ones, except for the nanoimprint step (Figure 2.2c). This design will serve to check that the performances are not degraded during the complex steps of bonding and substrate removal, and to evaluate the impact of a mirror on J_{sc}.

2.2 Process development

The previously detailed process has been elaborated and improved during the project, and it is still under development for some steps. Many steps are the result of long periods of process development, with many tests. In this section we describe the process development of three of those steps.

2.2.1 Adhesion of the Ag mirror

A key parameter for a physically deposited metal is its adherence to the material it is in contact with. If it does not adhere enough, it is common to add another metal layer in between which exhibits better adhesion properties, such as chromium or titanium.

This issue is investigated in the case of a cell transferred onto a flat silver mirror, without nanostructures (design also sketched in Figure 3.1b. So the adhesions that matter are at the $Al_{0.4}GaAs$/silver interface and at the silver/polymer interface. 4 samples are prepared from the C2853 wafer. The GaAs contact layer is etched to leave only the AlGaAs, and different adhesion layers are tested as shown in Table 2.1 and 2.2.

As for the $Al_{0.4}GaAs$/silver interface (Table 2.1), three different layers are tested : 7 Å of chromium, which is a pretty standard adhesion layer for metal deposition, but as it absorbs light, it would lower the reflectivity of the mirror, and it is also susceptible to diffuse in the adjacent layers. 10 Å of Germanium are tested which is supposed to be less prone to diffusion. And finally, an absence of adhesion layer is also tested.

To evaluate if the adhesion is effective and would hold at least for the rest of the process, and preferably over the cell's lifetime, a *tape-test* is performed. Standard tape is stuck on the silver and abruptly removed with a force applied approximately perpendicular (right angle) to the test area. The surface is then examined and if there was not any material remove by the tape, the adhesion is commonly admitted to be sufficient [20].

The result of this test was positive for all samples. Not adding any extra layer has the advantage to ensure the preservation of the best optical properties for the mirror, so this is the solution chosen.

Sample name	C2853-4	C2853-5	C2853-6
Layers	Ag (200 nm)		
		Ge (10 Å)	Cr (7 Å)
	AlGaAs		

Table 2.1: Adhesion layer tests between the AlGaAs and the Ag for 3 test samples (c2853-X are the names of the samples)

As for the adhesion at the silver/polymer interface (Table 2.2), the silver is either coated with 10 nm of chromium, or not coated. In both cases, the adhesion is evaluated during the substrate removal process, when the sample is immersed successively in three chemical solutions, the first one being exothermic (usually around 70 °C). At the end of this process, the backside of the samples is observed with the optical microscope and indications such as a peeling-off, a color change or a dissolution of the mirror would indicate that the adhesion of the polymer is not optimal.

The results are harder to interpret. Both samples are etched too much in the solution. The solution has infiltrated the ormostamp with two different mechanisms. The first solution, not selective, has etched all the way through the sample down to the mirror. Consequently to this, the chemicals were able to diffuse in the polymer and it started to lose its adherence. Another mechanism that occurred was the polymer not covering perfectly the sides of the sample, allowing diffusion through the sides.

It is likely that these problems are due to the choice of the samples. They are indeed small pieces on the border of the epitaxial wafer. during the epitaxy, a small band at the outer limit of the wafer is not grown as it is in contact with some holders in the chamber. It leads to a non uniform thickness of the whole stack at the edges, which could ease transverse diffusion of chemicals. The size of the samples is also detrimental to the test. They measure 0.3 cm^2 each, whereas the sample used for making solar cells correspond to 1.2 cm^2. This could have caused an uneven repartition of the polymer during the transfer, making them less stable mechanically.

As the main problems come from the substrate removal process itself, and the samples stay bonded despite the chemical issues, we concluded that this adhesion layer is not critical. A chromium adhesion layer will still be adopted for two reasons. First, to prevent the silver from oxidizing as it leaves the deposition chamber. Second, because there might be long-term stability issues with the silver directly in contact with the polymer, whose properties are not well known.

Sample name	C2853-4	C2853-5b
Layers	Ormostamp	
	Cr (10 nm)	
	Ag (200 nm)	

Table 2.2: Adhesion layers tests between the Ormostamp©polymer and the Ag for 2 test samples

In the end, the process for the mirror deposition is chosen as the successive deposition of 200 nm of silver and 10 Å of chromium with EBPVD, with an angle of 30 °with respect to the vertical axis to ensure conformal deposition.

2.2.2 Substrate removal : chemical or mechanical?

As for the substrate removal process, and due to some issues previously mentioned about the stability of the polymer interface, a mechanical polishing process is considered as an alternative process to a chemical etching. Let's first explain in details the chemical etching process and the issues during it. This chemical substrate removal consists in 3 successive wet etchings, to remove the 400 μm thick GaAs wafer, and reach the etch stop layer. The three solutions are :

1. $H_2SO_4 : H_2O_2 : H_2O$ with dilution 2:1:1. Not selective etch of GaAs from AlGaAs. Temperature kept above 70 °, and stirred with a magnetic stirrer. The etch rate for GaAs is about 15 μm/min. The sample is kept 20 minutes in this solution.

2. NH_4OH : H_2O_2 with dilution 1:19. Selective etch of GaAs from AlGaAs. Stirred with a magnetic stirrer. The measured etch rate for GaAs is about 4μm/min. The sample is kept in this solution until the first glimpse of the etch stop layer becomes visible.

3. $C_6H_8O_7(1g/mL) : H_2O_2(30\%)$ with dilution 5:1. Very selective etch of GaAs from AlGaAs : the etch rate for GaAs is $0,314$ μm/min, and 0.0027 μm/min for $Al_{0.3}$GaAs (tabulated rates from [19]). The sample is kept in this solution until the full removal of the GaAs substrate.

The setup for this etching process is the sample suspended in a beaker with a pair of tweezers so that the sample is kept dipped in the solution. A magnetic stirrer is rotating at 300 rotations per minute inside the beaker.

A key issue of this process is the uniformity of the etching. Due to turbulences inside of the beaker, the diffusion of the chemical species involved in the chemical reaction is anisotropic, and some areas are etched faster than others. To limit this effect, the sample is regularly rotated by a quarter turn, but there are still non-uniformities.

Another important issue is the presence of residual GaAs on the sides of the wafer. This is again due to the turbulence effects, and it is favored by the presence of polymer residues on the sides of the sample. Indeed, during the bonding process, when the sample is glued to a glass substrate with the polymer, some spreads on the sides of the sample. As it is not etched by the chemical solution, it leaves thin walls on the sides of the samples, that alter the local etch rate. See Figure 2.4.

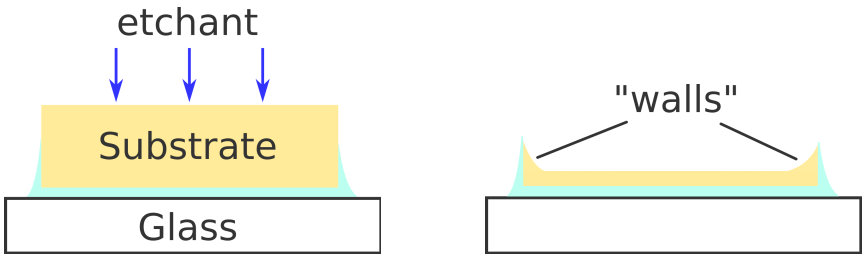

Figure 2.4: formation of side 'wall' residuals during the substrate removal process.

This is a problem for the rest of the process, the mask for the UV lithography needs to be *hard-contacted* to the sample, and those sort of walls around the sample would prevent a perfect contact.

The mechanical polishing process consists in fixing the sample to a heavy metallic puck, and gently rubbing this puck on a mill plate, covered with a solution containing alumina marbles, whose thickness is known (1 μm large particles were used).

It is a fast, non selective etching step, similar to the first solution of the chemical etching. Afterwards, it is necessary to finish the substrate removal with the last two solutions anyway, to ensure a selective stop.

It is expected to be more uniform than the first solution, faster, and more uniform, especially at the sides of the sample, where there is some polymer making thin 'walls'.

The conclusions of this comparison are straightforward:

- For both techniques, the surface is not etched uniformly, and the sample must be kept in the third solution for some time to compensate for this non-uniformity (40 minutes in the case of the polished sample, and 1 hour, 10 min for the fully chemically etched one).
- Both techniques leave much thicker residues close to the edges (walls about 100 μm thick) that obstruct the mask alignment during the later lithography steps. This is not critical though.
- The polishing technique takes much more time and requires some experience with chemical polishing as it is quite touchy.

As a conclusion, the chemical process has been adopted, due to its simplicity compared to the other one. The polishing did not overcome the issue of the thicker substrate residues at the sides due to the polymer 'walls', which was the main reason why this technique was considered.

2.2.3 Sol gel : reducing the strains during the thermal dehydration of the photo-resist

We now consider the process step after the nanoimprint, when the TiO_2 is etched away from the contacts, before mirror deposition (Figure 2.2c and 2.2d). To do so, a photo-resist is spin-coated on the TiO_2 to perform a negative UV-lithography and open the localized contacts. The TiO_2 on those contacts is then etched away.

The first nanoimprinted samples exhibit defects after the coating of the photo-resist. More precisely, cracks have appeared in the TiO_2 layer during the annealing of the photo-resist, see Figure 2.5. Those are most likely due to the strains induced by the thermal contraction of the resist as it is adsorbing its solvents. From this observation, two major defects could be identified in the TiO_2 sol-gel used.

First, there is strain in this material. The solidification of the sol-gel is a process during which a lot of matter escapes the material. Solvents desorb from it, through the porous structure of the TiO_2, at a temperature of 110 °. This annealing temperature is too low to form a crystalline structure, and such solidified sol-gel are often considered as amorphous. The strain existing in the solid would then relax due to the extra constraint induced by the resist shrinking while it is annealed at 125 °.

Second, the adhesion between the sol-gel and the underlying AlGaAs surface might not be perfect, and the sol gel is not maintained firmly enough on it. Indeed, such cracks did not appear with the same sol-gel on a different substrate, with silicium instead of AlGaAs.

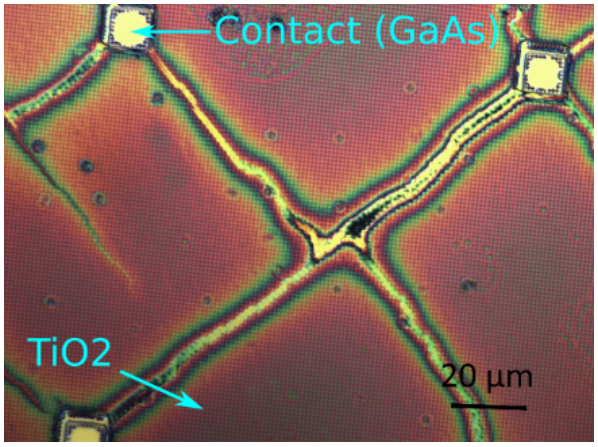

Figure 2.5: Cracks in the TiO_2 nanostructured layer.

Three different solutions are explored in order to limit this effect.

- The use of another photo-resist. Indeed, the first resist used (AZ5214) makes for thick coatings (about 1200 nm thick). The ma-N 2403 allows for film thicknesses down to 120 nm with an appropriate rotation speed during the spin-coating. The thinner the resist, the weaker the force applied to the underlying TiO_2 structure when it shrinks.

  Another advantage of the ma-N 2403 resist is that it does not need an additional annealing for the cross-linking, whereas the AZ5214 needs one. And the first annealing temperature is supposed to be 90 °, lower than 125 °for AZ5214. A lower temperature could generate less strain.

- The control of the temperature is a second point. If the temperature is raised more slowly during the annealing, we expect the shrinkage of the resist to be smoother and more uniform in the thickness of the layer. It would give it more time to relax as it desorbs its solvents.

- Finally, by changing the composition of the sol-gel solution, a better control over the strain could be attained.

The development of this process is still ongoing and is not completed at the time when this report is written. The ma-N resist has been tested and shows promising results on silicon samples, that still need to be transferred to AlGaAs samples patterned with TiO_2 structures. A test has been done about the control of the temperature ramp during the annealing. An AlGaAs sample patterned with TiO_2 has been coated with AZ5214 resist and annealed at a lower temperature (90 °instead of 125 °) but for a longer time. The patterned has been successfully developed, and even though there are still many cracks, they look thinner than previously.

By combining the approaches exposed above, we expect a positive result without any cracks by the end of the project, in two month.

In this second part, the detailed structure of the cells and their fabrication have been presented. As it is a long and quite complex process, we showed that many steps need to be developed before actually making a working device. As some of those process steps are still under development, we cannot yet make the final solar cell, but two simplified solar cells have been fully processed and can thus be characterized.

Chapter 3

Results and discussions

Three different designs of cells have been investigated in this project. The first one is as-grown (3.1a), another is transferred onto a flat mirror (3.1b), and the last one is transferred onto a nanostructured mirror (3.1c), but has not been fabricated yet. For this analysis, the fabricated solar cells do not have any Anti-Reflection-Coating (ARC), as presented on the sketches below. As a consequence, the measured J_{sc} and efficiencies could still be easily improved and correspond to state-of-the art performances, as it will be discussed in the last section of this chapter.

I have fully characterized the two first cells using the methods described in Apendix B. About 25 diodes have been measured on each sample, and as they exhibit similar performances, with a very small divergence, the results of the best representative diode for each sample are presented in this part.

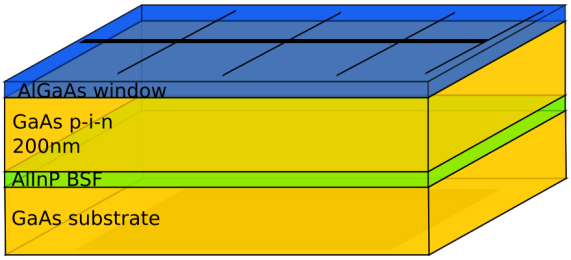

(a) Simple, "as-grown" cell, still on its substrate. (C2853-1)

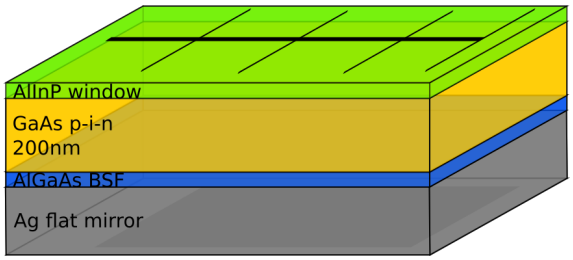

(b) Cell transferred onto a flat silver back mirror (C2853-3)

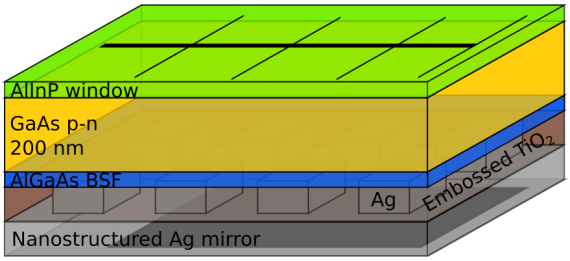

(c) Cell transferred onto a nanostructured silver back mirror

Figure 3.1: Designs of the three different cells realized, not yet coated with an Anti-Reflection Layer (ARC). Based on [7]

3.1 A simple solar cell on its substrate

The first cell fabricated follows the simplest design, as-grown, sketched in Figure 3.1a. The layers are not transferred onto an external glass substrate, and the contacts are directly patterned on top of the stack, and under the substrate.

Figure 3.2 shows an image of the top face of the device. The diodes with different sizes (A, B and c) have all been characterized and present very similar performance, with differences below the measurement uncertainty. But some cells present notably different electrical performances, often due to locally degraded contacts.

We will first discuss the optical performances of a representative diode of this sample, and then get into the electrical ones.

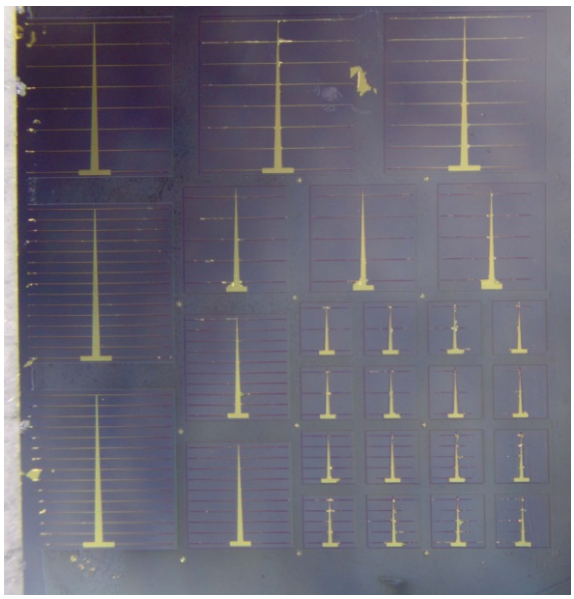

(a) Top view of the device.

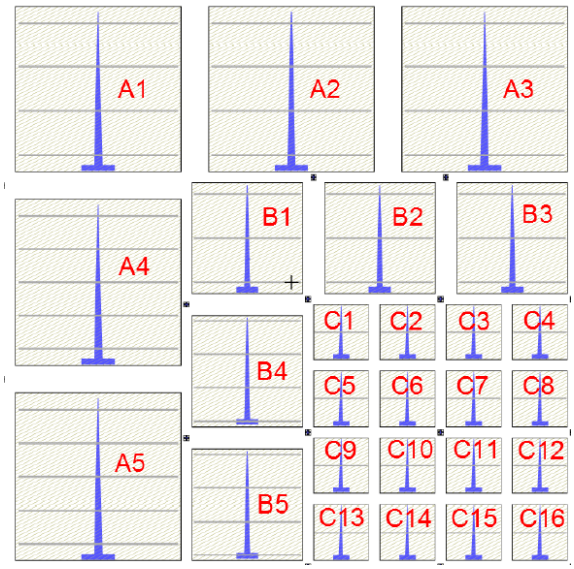

(b) Designation of the diodes.

Figure 3.2: Binocular microscope image of the as-grown cell and designation of the diodes.

3.1.1 Optical performances

The External Quantum Efficiency (EQE) is measured with the monochromator setup and plotted in Figure 3.3a. A value of the short-circuit current is also displayed, integrated from the EQE with the formula (1.3). In order to better discuss its shape, it is compared with another cell (Figure 3.3b), from a different epitaxial layer. The design process was the same though.

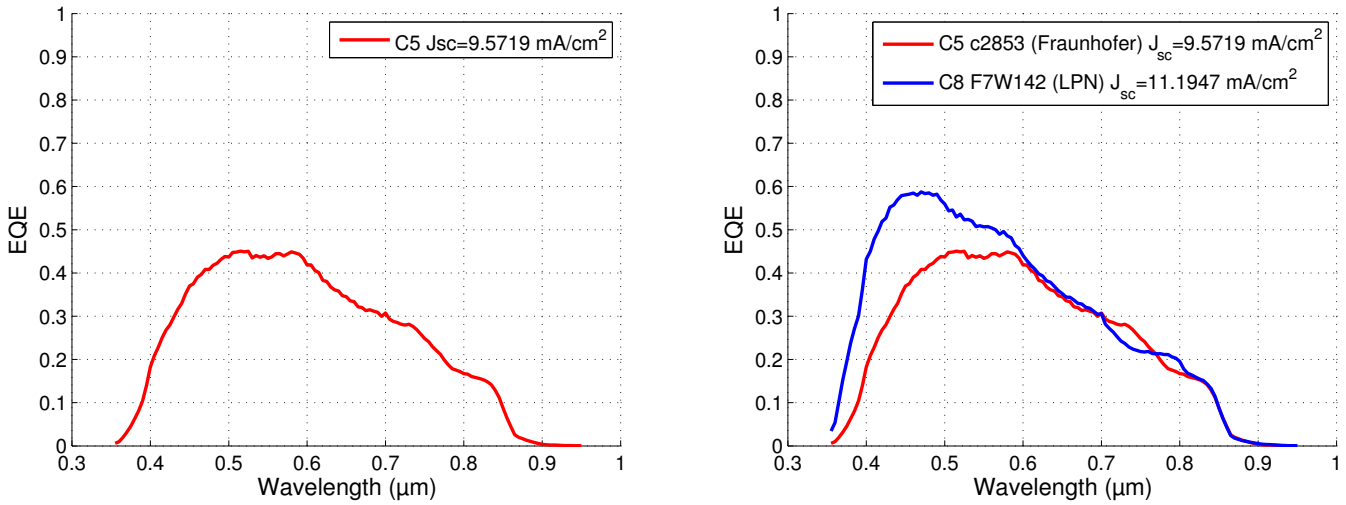

(a) External Quantum Efficiency of an as-grown cell, measured with the monochromator setup.

(b) Comparison with the EQE of a cell from another epitaxial stack.

Figure 3.3: External quantum efficiency of an as-grown cell, and comparison with another type of epitaxial layers.

As it can be seen, the curves are similar. There are some oscillations around 750 nm that differ slightly between the two curves. They could be resonating features, e.g. Fabry-Pérot, and their mismatch would come from the difference of thickness between the layers.

But the major difference is at smaller wavelengths, below 600 nm. The cell from the wafer F7W142 is optically different from the studied cell (wafer c2853) mostly because of its window layer (see Figure 3.4) which is a 35 nm thick AlGaAs window, with gradual aluminum content, up to 80 %. The c2853 stack was designed to be transferred onto another substrate, so the 100 nm thick $Al_{0.4}Ga_{0.6}As$ 'back surface field' layer acts as a window layer in this configuration. It is much thicker than the other one, and it has a smaller bandgap due to the lower aluminum content. As a consequence, the light that passes through this layer is more absorbed. It is not a region where carriers are expected to be collected, so this extra-absorption in this layer would translate into a loss on the EQE curve. This loss is present only at low wavelengths because it is the most energetic part of the light spectrum which is absorbed first, according to the expression of α, the absorption coefficient in Beer-Lambert's law of absorption [9] :

$$\alpha = \frac{4\pi \cdot \mathrm{Im}(\overline{n})}{\lambda} \qquad \text{in} \qquad I(x) = I_0 \cdot e^{-\alpha x} \tag{3.1}$$

Where $\overline{n}$ is the complex refractive index of the medium, and x represents the depth inside the medium. With this formula, the typical diffusion length in $Al_{0.4}Ga_{0.6}As$ at a wavelength of 400 nm is $\frac{1}{\alpha} = 21\ nm$, so most of the signal is absorbed in the 100 nm thick layer. Moreover $Im(\overline{n})$ is larger at smaller wavelength (1.5 at 400 nm) and decreases quickly (0.2 at 600 nm) (Refractive index data from [21]), which explains why both curves fall down quickly at small wavelengths.

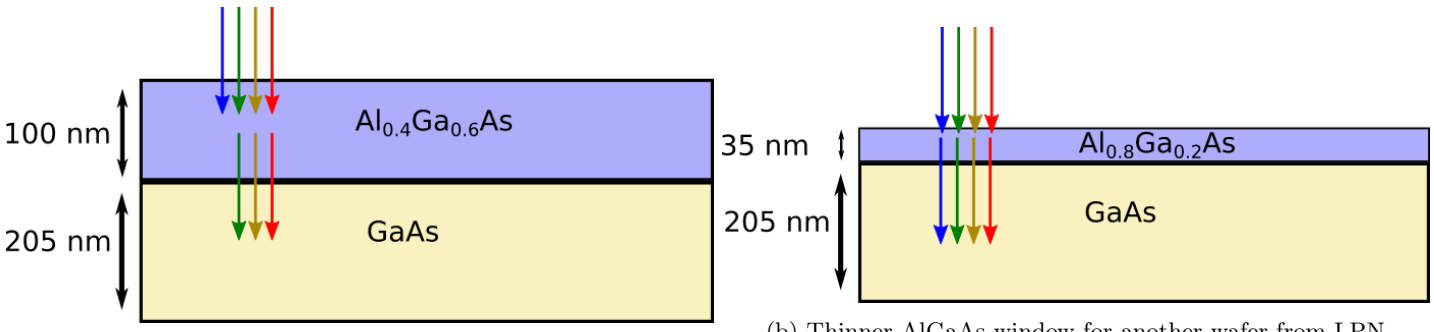

(a) Thick AlGaAs window for the c2853 wafer

(b) Thinner AlGaAs window for another wafer from LPN

Figure 3.4: Influence of the window's thickness on the absorption of the blue light

But we actually expect the red graph to be even lower comparatively to the blue one. According to Beer-Lambert's law, at a wavelength of 400 nm, 67 % of the light is absorbed in 21 nm of AlGaAs. After travelling through a 100 nm thick layer, we expect almost all of it to be absorbed in AlGaAs, but there is still an EQE about 0.2 at this wavelengh. This effect can be discussed with the help of the numerical simulation of the absorption in the different layers (Figure 3.5).

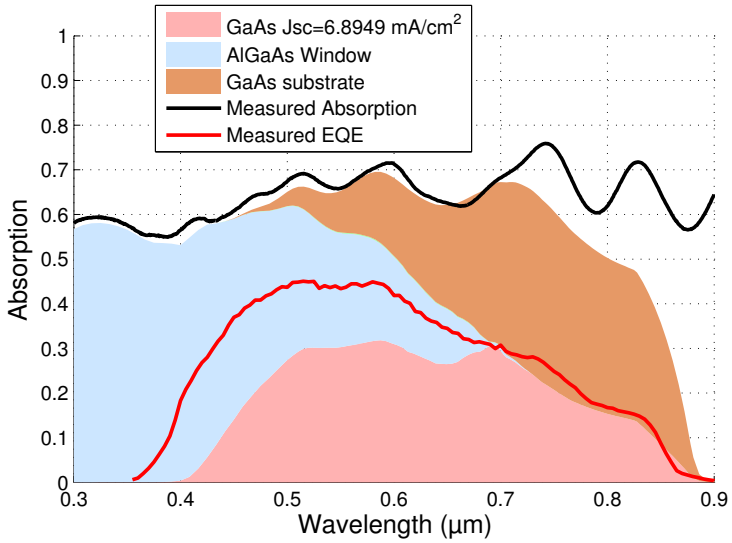

Figure 3.5: Simulated absorption in the different layers of an as-grown solar cell (filled areas). The absorption contributions are summed up so that one can easily read the total absorption. The measurements are also plotted as solid lines.

The absorption in the thin AlInP layer is so small that it is not visible on the graph.

The measured total absorption is consistent with the simulation. Indeed, by adding up all the simulated absorption contributions from the different layers, one reproduces the measured absorption with good fidelity at wavelengths below 700 nm. For longer ones, it is normal that the measure line is above the simulation. It comes indeed from a reflectivity measurement, and is simply $Abs = 1 - R$. The transmitted signal is not taken into account, but below the GaAs energy gap ($\lambda \geq 870\ nm$), the light is actually transmitted and would escape the substrate by the back side.

As for the absorption in GaAs, it should be concordant with the EQE curve, according to the discussion about the formula (1.4). But it is clearly under the EQE for wavelength below 700 nm. As previously found, the EQE seems boosted in this spectral region. This might indicate that carriers are collected outside the pn junction, in the AlGaAs window. This would allow for even higher photo-currents than expected. This is consistent with the fact that absorption in the AlGaAs (blue area) is quite high below 700 nm. As a consequence, the experimental J_{sc} (integrated from the EQE with equation 1.3) is higher than the one from the simulation (9.6 mA/cm^2 vs 6.9 mA/cm^2).

3.1.2 Electrical performances

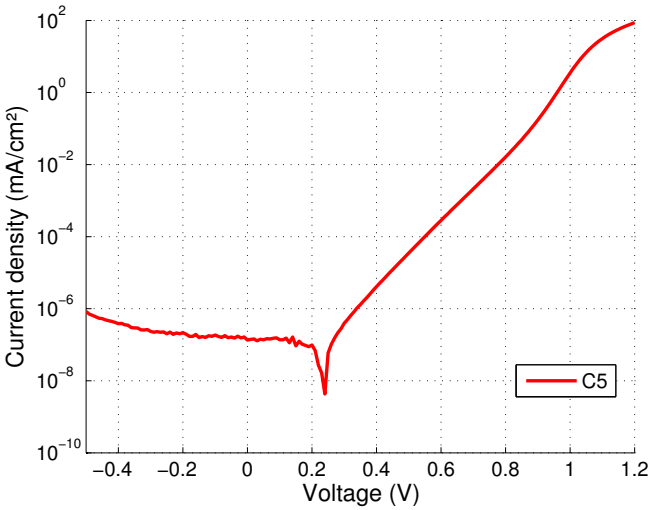

(a) IV curve in the dark (logarithmic scale on y-axis)

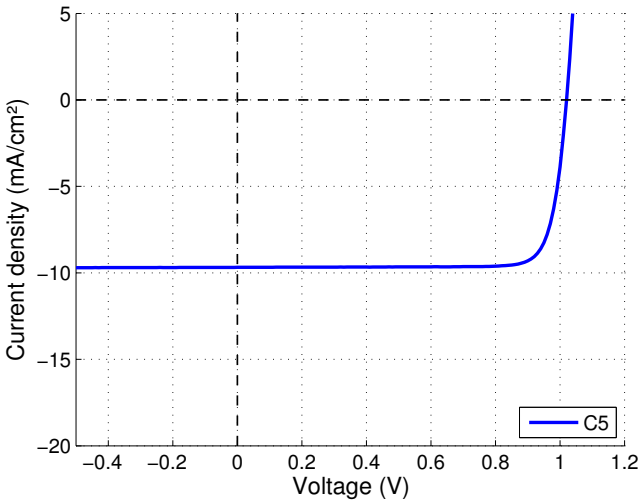

(b) IV curve under a '1 sun-like' illumination from a lamp.

Figure 3.6: IV curves of an as-grown cell

On the IV dark curve (Figure 3.6a), the logarithm of the absolute value of the current is plotted versus the voltage. The intensity is expected to be zero when no voltage is applied, because there is no photo-current then. But the curve exhibits a minimum in absolute value around 0.25 V. The room in which the experimental setup is is not perfectly dark and the remnants of light are enough to excite the diodes. Although it is a limitation for the experiment, it is encouraging as this effect was never seen before and it suggests low saturation currents. Indeed, with a low J_0, the derivative of the current with respect to the voltage is low as well, and a slight change in current induces a large shift in voltage.

More information can be extracted from this curve, if we make a fit with the double diode model. This was done using the software *2/3 diode fit* (Stephan Suckow, 2/3-Diode Fit (2014). http://nanohub.org/resources/14300). With this fit, we can now focus on the diode ideality (see Figure 3.7). The first diode in the model has an ideality set to 1 while the other's ideality is a free parameter in the fit. We can then display the current flowing through the two diodes of the model (and the shunt resistance, but it is negligible in this range).

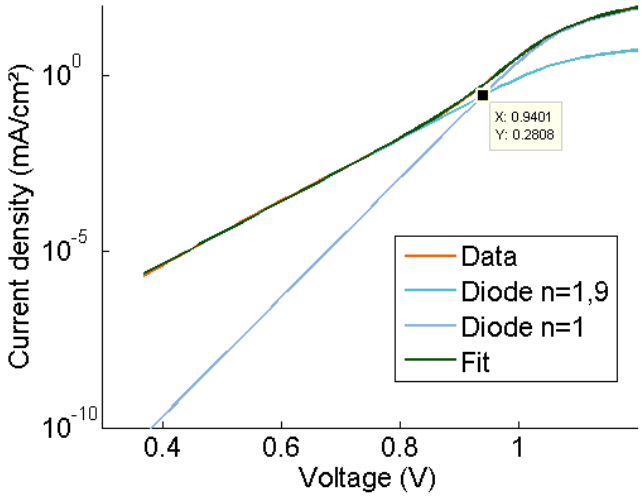

Figure 3.7: Fit of the previous IVdark characteristic with the double-diode model. The current flowing through each diode is also plotted.

The fit of this IV curve in the dark is very close to the experimental data and the curves are superimposed on the graph. At low voltages the current flows mostly through the diode whose ideality is close to 2, and then to the one whose ideality is 1, which is expected from the definition of the ideality. It is interesting to notice the point where the current starts to flow mostly through the diode n=1. We aim to have our open-circuit voltage where n=1, because an ideality close to 2 is often associated with non-radiative recombinations in the depletion region, and there are detrimental to the current that can be extracted. As the open-circuit voltage is $V_{oc} = 1.02\ V$, the device is expected to work in the regime of recombination with n=1.

But it is not straight-forward to transfer this conclusion to the operation of a real device under illumination. The superposition approximation, exposed in section 1.1.2, states that the IV curve under illumination is the IV curve in the dark, simply shifted by a constant term corresponding to the photo-generated current. However this does not hold for most actual devices. For example, we could not fit the IV curves under illumination with the double diode model.

The analysis of these 'IV-dark' curves is still very useful as it allows a comparison between different devices in conditions easy to reproduce (darkness).

From the fit, the EQE and the IV characteristic at one sun, many important parameters can be extracted. They are exposed in Table 3.1, first row.

The V_{oc} is especially high. Since it is in the area where the diode with an ideality of 1 dominates, we can use the formula (3.2). It comes from the current equation (1.1) when a diode dominates, and when the resistance effects are limited:

$$V_{oc} \approx \frac{kT}{q_0} ln\left(\frac{J_{sc}}{J_0^{n=1}}\right) \tag{3.2}$$

Thus, we expect to observe an enhancement of V_{oc} on the next cells realized, due to J_{sc} increasing from the mirror and the resonances, but also due to J_0 decreasing from photon-recycling effects ([22]).

The results for this solar cell 'as-grown' on its substrate are very encouraging, especially since the open-circuit voltage and the Fill Factor are high. The short-circuit current is still very low, which is

expected since there was no light-trapping strategy for this device, and it it too thin to collect most of the light during a single-pass. A key issue is to maintain all the other parameters equally good during the process of a transferred cell, to fully benefit from an increased photon collection.

3.2 A solar cell transferred onto a flat Ag mirror

This second cell is transferred onto a glass substrate, with a flat silver back mirror, as it is shown in Figure 3.1b. A picture of the finished sample can be seen in Figure 3.8. The designation of the diodes is the same as before.

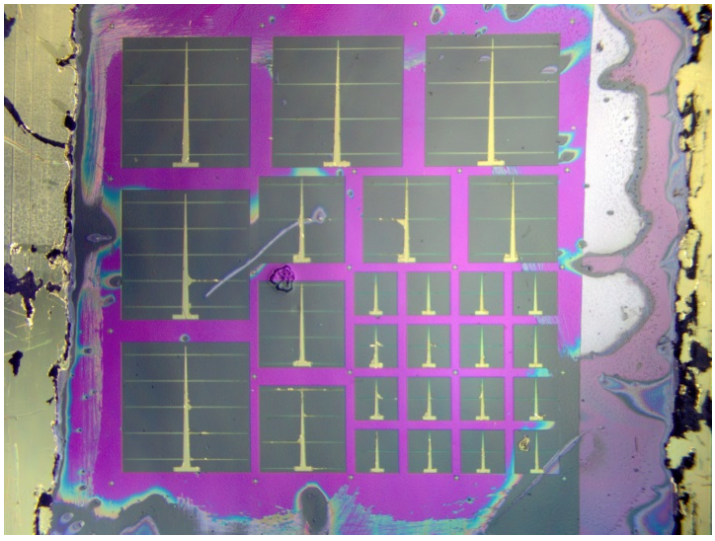

Figure 3.8: Top view of the device, transferred cell onto a flat Ag mirror.

3.2.1 Optical performances

Figure 3.9 shows the EQE of this transferred solar cell, compared with the one of the previous cell, as-grown. As the EQE spectrum presents two sharp resonant peaks, another method was used for the measure of the EQE, using the FTIR spectrometer (see Appendix B). The advantage is a better defined spectrum, especially with a highest maximum value of the peaks. The counterpart is that there is a lot of noise below 500 nm due to the light source which is weak away from the infrared. As a consequence, the curve was completed by the one from the monochromator setup, for all wavelengths below 550 nm. This discontinuity is visible on the curve.

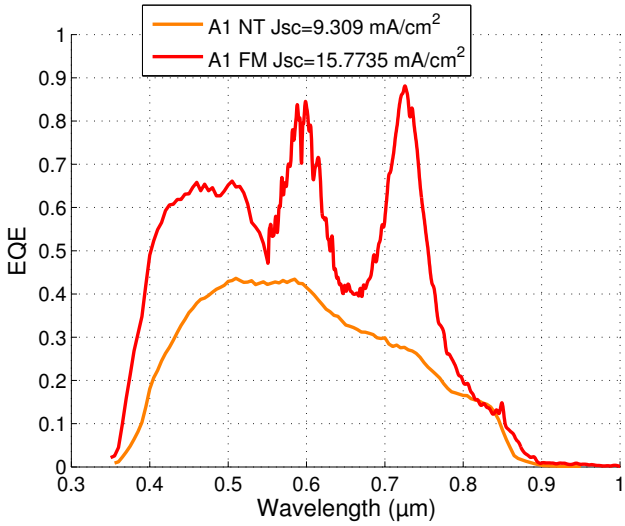

Figure 3.9: EQE of a cell transferred onto a Flat Ag Mirror ('FM'), compared with the one of an as-grown (Not-Transferred = 'NT') cell. The EQE of the FM sample (red) is measured with the monochromator setup for $\lambda < 550\ nm$ and with the FTIR setup for $\lambda > 550\ nm$.

There is a net gain of photo-current after transfer. Two Fabry-Pérot resonances are well visible at 590 nm and 720 nm. Apart from this expected result, there is also a gain below 500 nm, where the photons are expected to be collected within a single pass, so the mirror has no influence on their absorption. This can be explained by the asymmetry between the window layer and the back surface field layer on this wafer, as discussed previously (see Figure 3.4). The thick AlGaAs layer (100 nm) is now on the back of the sample, and instead, there is a thin AlInP layer (25 nm) which acts as a window layer. As a consequence, the light is less absorbed in this layer, and as the blue light is absorbed within a few tens of nanometers, it is in this range that an improvement was expected. Moreover, the energy gap of $Al_{0.6}InP$ (2.3 eV) is larger than the one of $Al_{0.4}GaAs$ (1.95 eV), making this layer transparent for even more light.

Let us now compare this measurements with the simulated absorptions. They are plotted in Figure 3.10, along with the measured absorption (A=1-R) and the previous EQE measurement curve.

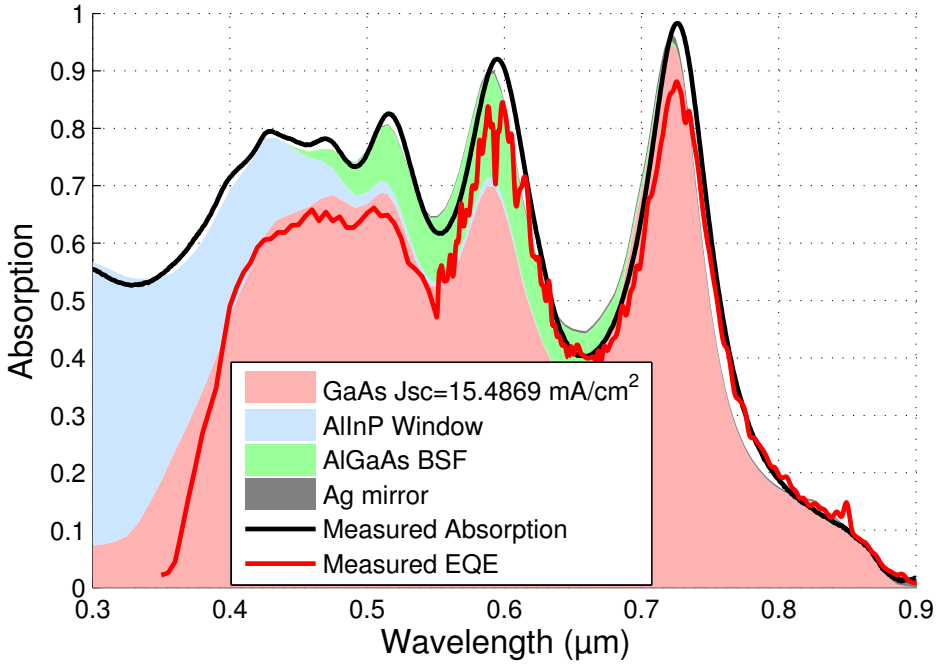

Figure 3.10: Simulated absorption in the different layers of a cell transferred onto a flat Ag mirror (filled areas). The measurements are also represented, with solid lines. The EQE was measured with the FTIR setup for wavelength above 550 nm, and with the monochromator setup for wavelengths below 550 nm.

It is interesting to notice the concordance of the measurements with the simulation, which seems to indicate that the numerical model for calculating the absorption is accurate. There is almost no absorption in the silver mirror due to its high reflectivity and poor absorption.

The collection of carriers seems to be almost perfect except at very low wavelength, below 400 nm where the EQE (red line) is lower than the simulated absorption in GaAs (red filled area).

It confirms that the IQE in our cell is close to 100 %. Surprisingly, the EQE is higher than the simulation between 550 nm and 650 nm. Similarly to the discussion about the previous cell, it would be that there is collection of the carriers generated the AlGaAs BSF. Indeed, as we can see on the filled green curve in Figure 3.10, there is a quite constant absorption in the AlGaAs between 500 nm and 650 nm, after which it goes to zero. An extra collection of the carriers generated in this layer would explain a boosted EQE in this range.

3.2.2 Electrical performances

Let us now discuss the IV characteristics of this solar cell.

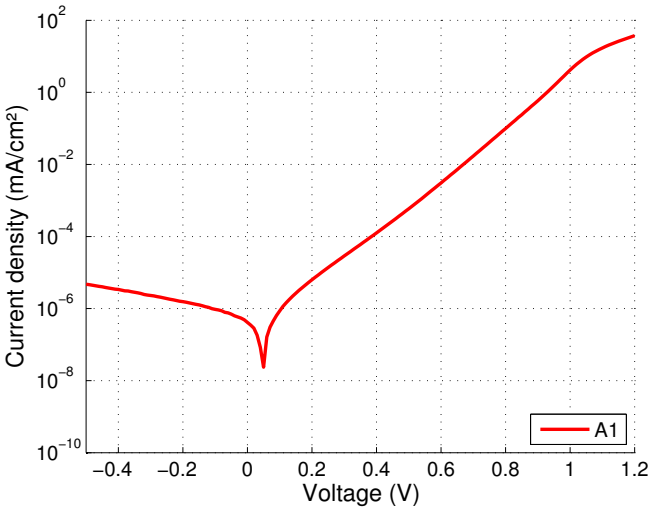

(a) IV curve in the dark (logarithmic scale on y-axis)

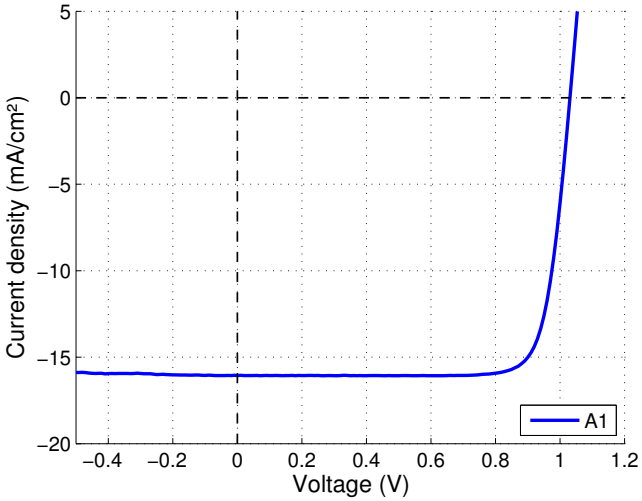

(b) IV curve under the solar simulator's illumination.

Figure 3.11: IV curves of a cell transferred onto a flat Ag mirror

The IV curve in the dark is very similar to the one for the as-grown cell. Again, one can see a slight shift of the zero because of the imperfect obscurity in the measurement room. As for the curve under an intensity of one sun, it confirms that the short-circuit current has improved a lot, while the open-circuit voltage and the Fill-Factor look similar to the ones of the previous sample (as-grown).

The dark characteristic was fitted to a double-diode model, and the evolution of the ideality can be discussed again (see Figure 3.12).

It appears that the regime changes for a slightly higher voltage than previously. Indeed, the current flows mostly through the diode whose ideality is 1 until V=0.99 V compared to V=0.94 V for the as-grown cell. As a consequence, the non-radiative recombinations are more likely to happen. But V_{oc} is still located above this transition voltage, so the recombination phenomena at the working voltage are still expected to follow an ideality of 1.

Again, those results can not be transferred easily to the device under illumination, because the IV curves under illumination could not be fitted with a double-diode model, and only the diode with ideality n=1 was impactful.

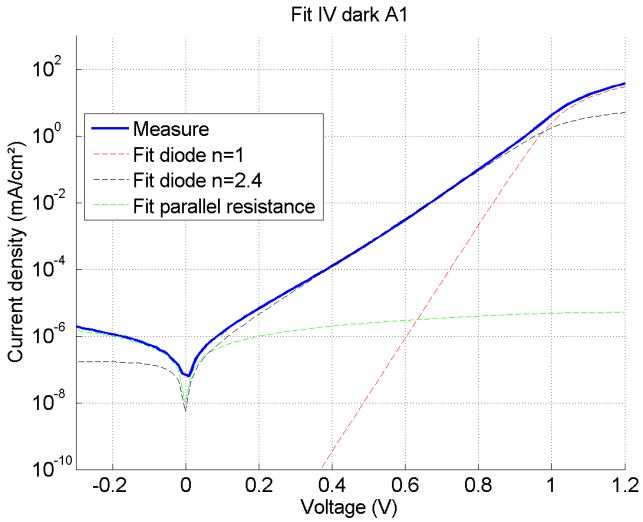

Figure 3.12: Fit of the previous IVdark characteristic with the double-diode model.

The IV curve under illumination is obtained with the solar simulator, which is supposed to emit a uniform AM 1.5G spectrum. It exhibits very high performances, which are exposed in Table 3.1 and will be discussed in the next paragraphs. One important particularity of this measurement is that the short-circuit current is J_{sc}=16.1 mA.cm^{-2}, higher than the one calculated from the EQE measurement, J_{sc}=15.8 mA.cm^{-2} (see Figure 3.9). It could likely come from measurement inaccuracies, for example if the peaks are not well defined, or because of the noise on the measurement, or because of the merging of the EQE curve from the monochromator setup with the one from the FTIR setup.

It could also originate from the approximation of the AM1.5G spectrum by the solar simulator. Indeed, as it is simulated with a lamp and some filters, some peaks or holes in the spectrum are not well reproduced. There is actually a deep hole in the AM1.5G at around 750 nm, which is not present on the solar simulator spectrum, in the datasheet provided by the manufacturer. As the biggest resonance peak of the EQE is at 720 nm (see Figure 3.10), the hole in AM1.5G could then represent a significant loss in the integration of J_{sc}, that is not taken into account by the solar simulator.

In any cases, the value extracted from the solar simulator experiment will be conserved for the discussion about the expected improvements with the nanostructures, section 3.3.

Parameter (Unit)	η (%)	V_{oc} (V)	J_{sc} (mA.cm^{-2})	FF (%)	R_{sh} (Ω·cm^2)	R_s (Ω·cm^2)	$J_0^{n=1}$ (A.cm^{-2})	J_{02} (A.cm^{-2})
NT	8.4	1.020	9.6 (EQE)	84.8	$2 \cdot 10^9$	1.3	$3 \cdot 10^{-20}$	$1 \cdot 10^{-12} (n = 1.9)$
FM	13.5	1.031	16.1 (IVsun)	81.9	$1.8 \cdot 10^8$	4.4	$6 \cdot 10^{-20}$	$2 \cdot 10^{-10} (n = 2.4)$

Table 3.1: Measured performance parameters of an as-grown (Not-transferred='NT') diode (C5) and a diode transferred onto a Flat Ag Mirror ('FM', diode A1). R_s, $J_0^{n=1}$ and J_{02} are extracted from the fit.

Those results are very encouraging, we can now discuss if the parameters have changed as expected compared to the as-grown cell, and the reasons why.

Since the cell is transferred onto the Ag mirror, it benefits from the Fabry-Pérot resonances and the increased light-path, which can be seen on the EQE curves. This explains the increase of J_{sc}, quite consistent with the numerical predictions.

The dark currents J_0 were supposed to decrease due to the mirror [22]. Instead, the saturation current for the diode of ideality n=1 increases by a factor 2. This is probably due to the fact that some defects were created in the layers or at the surfaces during the process, acting as recombination centers for the carriers. We can assume that if the process is further improved and better controlled, the saturation currents could be lowered.

It is difficult to compare the saturation currents for the second diode of the model, as the ideality has also changed.

As we showed that V_{oc} is still in a region where the ideality is mostly 1, the relationship (3.2) could still hold. Let us verify if the increase in term of V_{oc} is consistent with that. First, the effect of J_{sc} is:

$$\delta V_{oc} \approx \frac{kT}{q_0} ln\left(\frac{J_{sc}^{FM}}{J_{sc}^{NT}}\right) = 0.013\ V \tag{3.3}$$

Then, the effect of $J_0^{n=1}$ is:

$$\delta V_{oc} \approx \frac{kT}{q_0} ln\left(\frac{J_0^{NT}}{J_0^{FM}}\right) = -0.018\ V \tag{3.4}$$

The experiment shows an enhancement $\delta V_{oc} \approx 0.011\ V$. We cannot conclude for sure, because it looks like the effect of the larger $J_0{}^{n=1}$ was overestimated. It could be that the contribution of the diode with an ideality of 1 to the current is not really dominant, and the relationship is not valid. At least, there is an increase of V_{oc} and it has probably originated from the increase of J_{sc}.

But it is certain that, as Voc is at the limit between the two different recombination regimes, special attention must be paid to the control of the saturation currents. A low $J_0^{n=1}$ would ensure a low δV_{oc} but a low J_{02} must be maintained to ensure that the radiative recombinations dominate.

The shunt resistance has decreased a bit, but this is not significant since it is still high enough to have no impact on the Fill-Factor. But the increase in term of series resistance is detrimental to the performances, and could explain the deterioration of the Fill-Factor. It is likely due to some problems during the definition of the contacts. First, the development of the back contacts' lithography was not optimal and an important part of the localised contacts were missing after the lift-off (about half). Moreover, the front contacts were metalized two times because of a problem during the first metal evaporation.

The results on this transferred cell are very promising, especially since the open-circuit voltage and the Fill-Factor have maintained their high value despite the transfer process. This is very encouraging since the major limitation to the efficiency in the previous work of Nicolas Vandamme ([5]) was the degradation of those parameters during the transfer.

As for the numerical simulation, the good concordance between the simulated curves and the experimental ones seems to indicate that the numerical model is accurate, and sometimes even underestimates the external quantum efficiency, as we don't take into account collection in the barrier layers. We have high expectations for the cell with a nanostructured mirror based on the numerical simulations, as it will be discussed in the last part.

3.2.3 Influence of an ARC

Adding an Anti Reflection Coating (ARC) would increase even more the photo-current. This was not done experimentally yet, but the thickness was numerically optimized, and simulations were performed

to calculate the impact of such a layer on the absorption. This is presented in Figure 3.13, and the absorptions are compared with the ones calculated for the same geometry without ARC.

First, one can notice the modification of the peak shapes. This comes from the fact that the Fabry-Pérot resonator was modified by the addition of this extra layer. Since the Si_3N_4 refractive index is about 2 in the visible range (compared to about 4 in the GaAs, and 1 in the air), the coupling of light in the resonator is not the same.

The interesting consequence of an ARC is a net increase of the photo-current. The numerical absorption in the active layer rises from 15.5 mA.cm^{-2} to 19.7 mA.cm^{-2} with the addition of the ARC. This is an enhancement of $\delta J_{sc} = 4.2$ mA.cm^{-2} in the active layer. Thus, by adding an ARC to our device, we expect an enhancement of the efficiency to :

$$\eta_{ARC} = FF \cdot (Jsc + 4.2) \cdot V_{oc} = 17.1\%$$

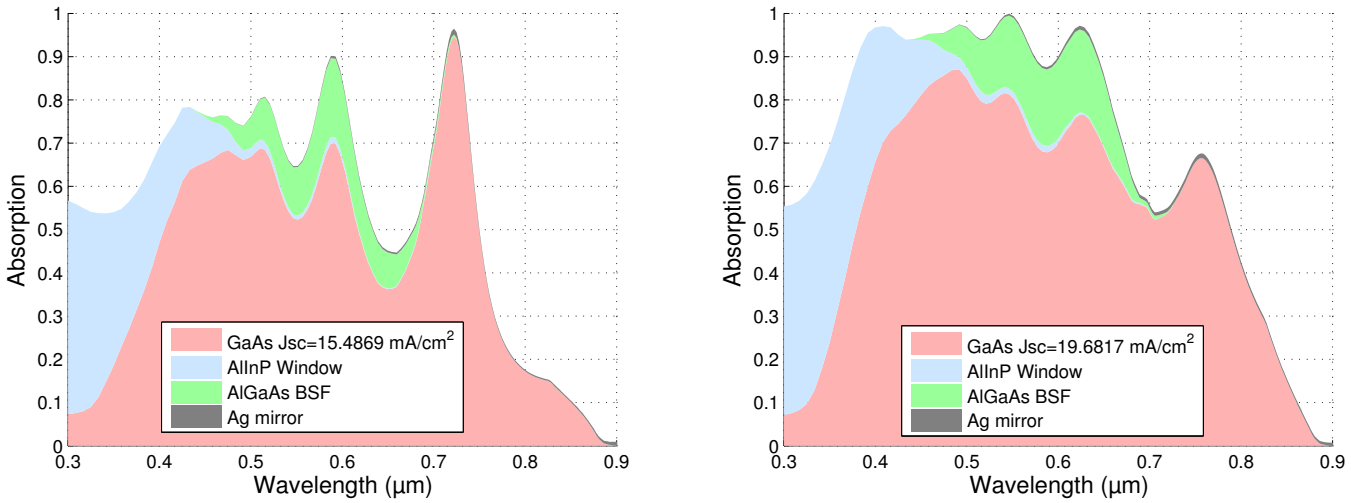

(a) Simulated absorptions in a solar cell transferred onto a flat Ag mirror.

(b) Simulated absorptions in a solar cell transferred onto a flat Ag mirror with an Anti Reflection Coating (ARC) on top

Figure 3.13: Influence of the ARC on the absorption in the cell transferred onto a flat mirror. Simulations.

Note that Si_3N_4 is used for the simulations, but during the deposition the proportions of Si and N are not perfectly controlled. Thus, we prefer to refer to it as SiN_X.

3.3 The solar cell on a nanostructured mirror

As of today, there is no sample to characterize since the process development has not been completed yet. However, the numerical results can be discussed and analysed in comparison to the previously made cells.

Figure 3.14 shows the simulated absorption in a cell transferred onto a nanostructured back mirror whose geometrical parameters (pitch, Length-Ratio and height) lead to the best absorption.

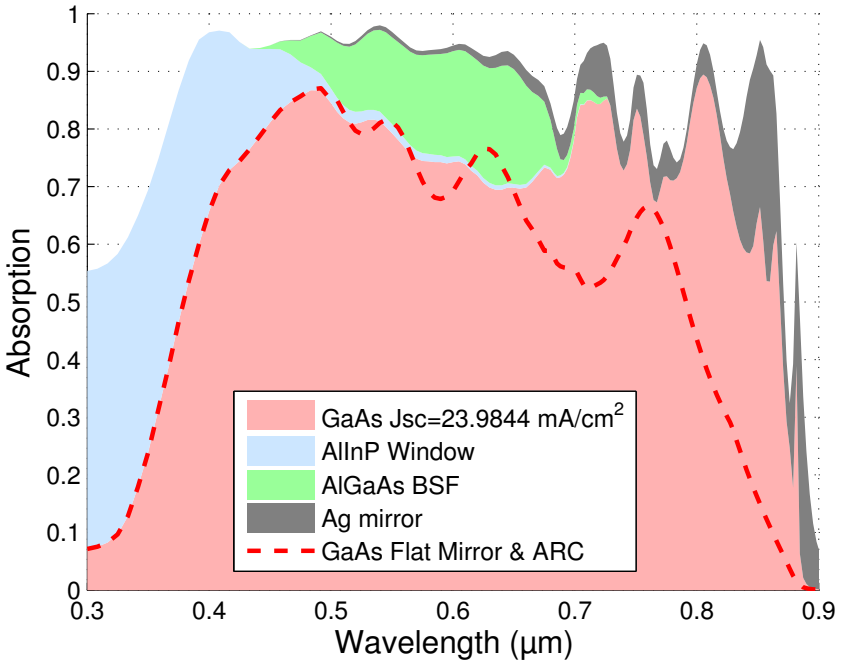

Figure 3.14: Simulated absorption in a cell transferred onto a nanostructured silver back mirror, with optimized geometric parameters and an Anti-Reflection-Coating. The simulated absorption in the previous geometry, with only a flat mirror and an ARC, is also plotted as a dotted red line.

Two bigger peaks in term of absorption can be seen, around 720 nm and 800 nm. They could originate from Fabry-Pérot resonances, as in Figure 3.13b where three Fabry-Pérot peaks were also visible. The other peaks, much less distinguishable as they overlap a lot, are other resonances (guided-wave, localized resonances, couplings of these resonances) and arise from the nanostructured mirror.

Due to the complexity of the structure, the numerical resolution needed a lot of time to be computed (many Fourier orders). There are still artifacts coming from the simulation, such as the high absorption in the silver, in the peak around 710 nm. Indeed, the resonances induce regions with a locally high electromagnetic intensity, which are often localized at the edges of the silver plots, in the nanostructure. If the resolution of the simulation is not high enough, it calculates this intense field inside the silver, whereas it is at the limit of it, but still inside the AlGaAs or the TiO_2.

The calculated absorption sports a high value in the GaAs active layer, at 24.0 $mA.cm^{-2}$.

This a net improvement of +4.3 $mA.cm^{-2}$ compared to the previous simulation without the nanostructures (dotted line)!

This enhancement is absolutely meaningful since it is of the order of magnitude of the improvement calculated when an ARC is added.

To relate that with the experimental measurements, let us come back to the previous results, on a flat mirror and without ARC. In this case, the simulated absorption in the GaAs layer was 15.5 mA.cm^{-2} (Figure 3.13a). So, numerically, the nanostructures combined with the ARC represent an enhancement of +8.5 mA.cm^{-2}. Of course, this holds solely if other parameters are not degraded during the process.

By taking the previous experimental efficiency and including this expected improvement of the short-circuit current, the short-circuit current and the efficiency could go as high as :

$$Jsc^{max} = Jsc + 8.5 = 24.6 \text{ mA.cm}^{-2}$$

$$\eta^{max} = FF \cdot (Jsc + 8.5) \cdot (V_{oc} + 0.011) = 21.0 \ \%$$

This would be a record for a GaAs solar cell with an optical thickness of 200 nm.

Conclusion

In this project, we wanted to make an ultrathin solar cell implementing an innovative light-trapping strategy, that would reach a record efficiency, never attained for such optically thin devices.

The potential of the multi-resonant absorption applied to ultrathin solar cells was first highlighted, and an optimized design for a solar cell with a periodic nanostructured mirror was proposed.

The process has been elaborated to implement the light-trapping nanostructures on an actual solar cell, but some specific issues are still under development, like the mechanical stability of the TiO_2 layer under external strain. However, a complete cell is expected to be realized soon, before the end of this project.

Based on the comparison between numerical simulations and experimental results with solar cells that only differ by the mirror's geometry, a record efficiency higher than 20 % could be reached. It is mostly due to a short circuit-current increased by $+4.3$ mA.cm^{-2} in the simulations with the nanostructures, with respect to the simulations of the same design with just a flat mirror.

It paves the way towards cheap ultrahin solar cells, as the process can be further optimized to avoid having a lot of semiconductor material which is then etched away (the substrate, the contact layers) and fully benefit from the light absorption in a 200 nm thin active layer. For example, Epitaxial Lift-Off (ELO) [23] can be implemented, and would allow to reuse the sample after the solar cell is peeled away from it.

Future work

In order to make the final solar cell, the development of the mechanical stability of the TiO_2 remains to be completed, as explained in the 'Process development' section. Two process steps remain to be developed as well. First, the adhesion of the mirror on the TiO_2 structures has not been investigated, but we will of course use the results and methods from the development of the adherence between the silver mirror and the AlGaAs. Then, the ARC deposition has not yet been done either. But this step was already done on similar samples with success, so there should not be that much development required.

The optical simulations are based on the optical index of each material to calculate their absorption. As of now, those parameters are mainly taken from databases of material properties (e.g. [21]) and could not match perfectly our own materials' indices. Ellipsometry measurements of our materials would give much more accurate indices for TiO_2 and SiN_X. Since TiO_2 is a sol-gel, its properties are unique and strongly depend on its preparation and its deposition.

The influence of the ARC could be evaluated experimentally on the two samples already made. Comparing the measurements and the simulations would help verify that the numerical predictions are accurate.

Appendix A

Software for the simulations of light absorption

All electromagnetic simulations presented used the Matlab program RETICOLO. It was developed by Philippe Lalanne and Jean-Paul Hugonin (Institut d'optique) and is based on the Rigorous Coupled Wave Analysis (RCWA) [24]. We will give a simplifeied explanation of this type of simulation.

A structure in RCWA consists in a stack of layers with specific refractive indices along a direction z and infinitely long and periodized in the xy-plane. It is excited by a plane-wave along the z-direction (see Figure A.1). The electromagnetic field as well as the structure are expressed as a Fourier series (plane-wave expansion). The Maxwell's equations are solved in the k-space inside of each layer, which comes down to solving an eigenvalue problem. A wave propagating in a layer can be expressed in term of the eigenfunctions of this equation (the eigenmodes of the layer). The amplitude coefficients of this wave expansion are placed in the vectors $\mathbf{s}^+$ or $\mathbf{s}^-$, depending if the wave is progressive or regressive. This procedure is applied for each layer of the stack, then boundary conditions are imposed at the interfaces between the layers. Continuity equations at these interfaces are solved with the help of a scattering matrix, S, which couples the $\mathbf{s}$ coefficients of each layer:

$$\begin{bmatrix} \mathbf{s_1^-} \\ \mathbf{s_2^+} \end{bmatrix} = S_i \cdot \begin{bmatrix} \mathbf{s_1^+} \\ \mathbf{s_2^-} \end{bmatrix} \tag{A.1}$$

Those scattering matrices can be combined to find a global scattering matrix:

$$\begin{bmatrix} \mathbf{s_e^-} \\ \mathbf{s_s^+} \end{bmatrix} = S_{tot} \cdot \begin{bmatrix} \mathbf{s_e^+} \\ \mathbf{s_s^-} \end{bmatrix} \tag{A.2}$$

$\mathbf{s_s^-}$ can be set to zero because there is no light incident from the substrate. It is solved and the $\mathbf{s}$ coefficients of the incident medium and the substrate can be determined.

Then, every $\mathbf{s}$ coefficients can be calculated using $\mathbf{s_e^-}$ and $\mathbf{s_e^+}$ and the intermediate combinations of scattering matrices.

Thus, the electric field is known everywhere in the structure.

The fact that the structure is expressed on a Fourier basis makes this method ideal for calculations of light scattering by periodic structures, which can easily be expanded as a Fourier series.

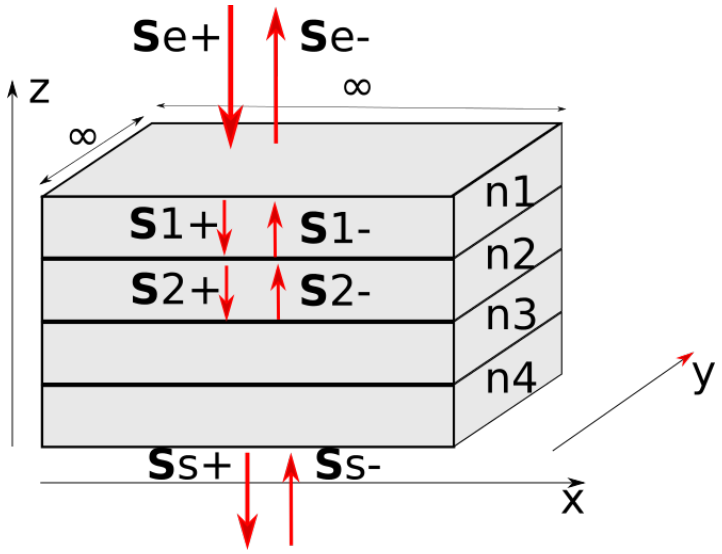

Figure A.1: Convention for the wave propagation in the RCWA method

Appendix B

Characterization tools

The characterization at LPN consisted in analyzing the solar cells with different experimental setups, allowing to draw IV curves in the dark or under a standard solar illumination, or wavelength resolved EQE and absorption spectra. Those tools are described in [5].

Absorption measurments

The total absorption of a cell is obtained via a measure of their reflection at normal incidence. The reflection is normalized by the reflection of a known SiO_2 sample, taking into account the background noise. It is performed with a Sentech reflectometer RM2000, with two light sources, deuterium and halogen. They allow to measure reflection in the 300-1000 nm wavelength range, useful with GaAs absorbers.

The IV setup

A source monitoring unit (SMU) is used for electrical measurements. It is a Keithley Sourcemeter.

The contacts are placed on the sample with a pair of needles, in a four-point probe configuration (see [10] for further description of this configuration). They allow to deliver a voltage and measure the current photo-generated in the cell. The first pair of points is placed on the front annular contacts, and the other is connected either to the back mirror, which incorporates the localized ohmic contacts, or on the rear side of the substrate in the case of an 'as-grown' cell.

The SMU signal is transmitted to a computer with a homemade software to draw the IV curves. They can be drawn in the dark or under illumination. In the dark, all light in the room are shut down, but the sample is not completely isolated from parasitic illuminations, as discussed in section 3.2.2.

EQE measurements with a monochromator

The External Quantum Efficiency (EQE) is the probability of collecting an electron from a photon, and it is determined at each wavelength. The first setup to get EQE curves is a Xenon light source sent toward a blazed grating with a 350-950 nm range. The light beam transmitted is a spectral peak centered around a certain wavelength, with a width controlled by the diameter of the exit slit of the monochromator. With a fully open slit, which was our configuration, the spectral width at half maximum amounts to 10 nm, but it allows for a high signal intensity, thus reducing the signal-to-noise ratio.

In parallel with the optical line, a source monitoring unit (SMU) is used for electrical measurements. It is a Keithley Sourcemeter. It delivers a voltage (V=0 V for the EQE setup) and measures the current

photo-generated in the cell.

The measurement procedure consists in two steps. First, a wavelength scan is run over the 350-650 nm spectral range and the current delivered by a calibration diode at zero bias is recorded. Then, the same scan is run on the sample to be tested. As the EQE of the calibration diode is known from its responsivity, the EQE of our cell is simply deduced as the ratio:

$$EQE(\lambda) = EQE_{ref}(\lambda) \cdot \frac{J(\lambda)}{J_{ref}(\lambda)}$$

The short-circuit current is deduced from this experiment, by integrating the EQE, normalized by the AM 1.5 G spectrum, as shown in the formula:

$$J_{sc} = q_0 \int_0^{\infty} EQE(\lambda) \cdot \frac{\lambda \cdot \Phi(\lambda)}{h \cdot c_0} d\lambda \tag{B.1}$$

An inconvenient of this setup is that the gratings sometimes moves and loses its calibration so the signal is shifted by a few wavelengths.

EQE measurements with the FTIR

Another setup for calculating the EQE relies on the Fourier Transform Photocurrent Spectroscopy (FTPS), by using a Fourier Transform InfraRed (FTIR) spectrometer. In a FTIR spectrometer, the light passes through a Michelson interferometer, whose arms' length is variable. A signal with a path difference varying with time can then exit the source and hit the sample. The photo-generated current is measured with the SMU in real time. The interferogram thus displays the current versus the light path difference in the interferometer. A Fourier transform allows to obtained a signal as a function of the wavelength.

As for the method with the monochromator, the signal is normalized by the response of a calibration diode whose EQE is known.

The light source is an infrared lamp and its intensity decreases rapidly in the visible range. as a consequence, the signal-to-noise ratio is not high enough below 500 nm and the EQE can not be read anymore.

However, the spectral resolution is better than with the monochromator, and it is less susceptible to exhibit a spectral shift, allowing for more accurate curves.

IV curve with a 'one-sun-like' light source

A simple way to plot IV curves under illumination is to use a light source with a spectral distribution similar to the solar one. For this purpose, we used a tungsten lamp.

We showed that it was possible to extract a value for the short-circuit current from the EQE (1.3). As a consequence, when the sample is illuminated by the lamp, one can adjust the light intensity until the measured short-circuit current equals the one calculated from the EQE. In this configuration, the sample is placed under illumination conditions close to the one of a real solar simulator, and an IV curve can be plotted.

Useful parameters such as V_{oc} or FF can thus be extracted with quite high accuracy.

IV curve with a solar simulator

Some commercial systems are much more elaborated to reproduce solar illumination conditions.

The lab recently acquired a solar simulator that reproduces the AM1.5G spectrum with more accuracy. It is constituted of a powerful lamp in front of many filters that shape its spectrum. The collimation of the light is also very precise to ensure spatial homogeneity of the light intensity. As the intensity depends on the distance of the sample from the output lens of the simulator, the height of the lamp is set using a calibration diode whose short-circuit current under AM1.5G is known.

As this device was installed recently, only the second sample (transferred onto a flat mirror) could be measured with it. The results with this simulator exhibit a higher short-circuit current than the one calculated from the EQE, as discussed in section 3.2.1. This could originates from the placement of the sample with parasitic reflections by the platform or the tips, or from a problem of calibration of the height, as the setup is very knew and was not fully tested and verified. It could also be that there is a fundamental difference between those two measurements, as it is also discussed in section 3.2.1.

Bibliography

[1] B. M. Kayes, H. Nie, R. Twist, S. G. Spruytte, F. Reinhardt, I. C. Kizilyalli, and G. S. Higashi. 27.6cells under 1 sun illumination. In *Photovoltaic Specialists Conference (PVSC), 2011 37th IEEE*, pages 4–8, June 2011.

[2] Weiquan Yang, Jacob Becker, Shi Liu, Ying-Shen Kuo, Jing-Jing Li, Barbara Landini, Ken Campman, and Yong-Hang Zhang. Ultra-thin gaas single-junction solar cells integrated with a reflective back scattering layer. *Journal of Applied Physics*, 115(20), 2014.

[3] Sung-Min Lee, Anthony Kwong, Daehwan Jung, Joseph Faucher, Roshni Biswas, Lang Shen, Dongseok Kang, Minjoo Larry Lee, and Jongseung Yoon. High performance ultrathin gaas solar cells enabled with heterogeneously integrated dielectric periodic nanostructures. *ACS Nano*, 9(10):10356–10365, 2015. PMID: 26376087.

[4] Keisuke Nakayama, Katsuaki Tanabe, and Harry A. Atwater. Plasmonic nanoparticle enhanced light absorption in gaas solar cells. *Applied Physics Letters*, 93(12), 2008.

[5] Nicolas Vandamme. *Nanostructured ultrathin GaAs solar cells*. PhD thesis, Université Paris-Sud, 2015.

[6] N. Vandamme, H. L. Chen, A. Gaucher, B. Behaghel, A. Lemaître, A. Cattoni, C. Dupuis, N. Bardou, J. F. Guillemoles, and S. Collin. Ultrathin gaas solar cells with a silver back mirror. *IEEE Journal of Photovoltaics*, 5(2):565–570, March 2015.

[7] Chen et al. 200nm-thick gaas solar cells with a nanostructured silver mirror. In *EMRS spring meeting*, 2016.

[8] P. Würfel and U. Würfel. *Physics of Solar Cells: From Basic Principles to Advanced Concepts*. Physics textbook. Wiley, 2009.

[9] J. Nelson. *The Physics of Solar Cells*. Series on Properties of Semiconductor Materials. Imperial College Press, 2003.

[10] Stuart Bowden and Christiana Honsberg. *pveducation.org*. http://pveducation.org/, 2016.

[11] S.M. Sze and K.K. Ng. *Physics of Semiconductor Devices*. Wiley, 2006.

[12] Stéphane Collin. Nanostructures pour le pv. In *Journée thématique du C2N*, 2016.

[13] E. Yablovnitch. Statistical ray optics. *Journal of the optical society of America*, 1982.

[14] E. Yablovnitch. Intensity enhancement in textured optical sheets for solar cells. *IEEE Transactions on electron devices*, 1982.

[15] Malvin Carl Teich and BEA Saleh. Fundamentals of photonics. *Canada, Wiley Interscience*, 3, 1991.

[16] S. P. Tobin, S. M. Vernon, C. Bajgar, S. Wojtczuk, M. R. Melloch, A. Keshavarzi, T. B. Stellwag, S. Venkatensan, M. Lundstrom, and K. A. Emery. Assessment of mocvd- and mbe-growth gaas for high-efficiency solar cell applications. *IEEE Transactions on Electron Devices*, 37(2):469–477, Feb 1990.

[17] F. Dimroth, T. N. D. Tibbits, M. Niemeyer, F. Predan, P. Beutel, C. Karcher, E. Oliva, G. Siefer, D. Lackner, P. Fuß-Kailuweit, A. W. Bett, R. Krause, C. Drazek, E. Guiot, J. Wasselin, A. Tauzin, and T. Signamarcheix. Four-junction wafer-bonded concentrator solar cells. *IEEE Journal of Photovoltaics*, 6(1):343–349, Jan 2016.

[18] A.S. Gudovskikh, N.A. Kaluzhniy, V.M. Lantratov, S.A. Mintairov, M.Z. Shvarts, and V.M. Andreev. Numerical modelling of gainp solar cells with alinp and algaas windows. *Thin Solid Films*, 516(20):6739 – 6743, 2008. Proceedings on Advanced Materials and Concepts for Photovoltaics {EMRS} 2007 Conference, Strasbourg, France.

[19] A.R Clawson. Guide to references on iii–v semiconductor chemical etching. *Materials Science and Engineering: R: Reports*, 31(1–6):1 – 438, 2001.

[20] *Test Methods Manual, test method 2.4.1, Adhesion, Tape Testing.* IPC-TM-650. 2004.

[21] Edward D. Palik, editor. - *Contributor Index.* Academic Press, Burlington, 1985.

[22] O. D. Miller, E. Yablonovitch, and S. R. Kurtz. Strong internal and external luminescence as solar cells approach the shockley-queisser limit. *IEEE Journal of Photovoltaics*, 2(3):303–311, July 2012.

[23] G.J. Bauhuis, P. Mulder, E.J. Haverkamp, J.C.C.M. Huijben, and J.J. Schermer. 26.1 *Solar Energy Materials and Solar Cells*, 93(9):1488 – 1491, 2009.

[24] Philippe Lalanne and G. Michael Morris. Highly improved convergence of the coupled-wave method for tm polarization. *J. Opt. Soc. Am. A*, 13(4):779–784, Apr 1996.